**EUROPEAN JOURNAL OF PURE AND APPLIED MATHEMATICS**
2025, Vol. 18, Issue 3, Article Number 6505
ISSN 1307-5543 – ejpam.com
Published by New York Business Global

# Thermocapillary and Photocapillary Effects on a Spherical Droplet Embedded in a Brinkman Medium

A. S. Aamer[1], Baraa A. Ahmed[2], Samar A. Mahrous[2,*]

[1] *Department of Mathematics and Computer Science, Faculty of Science, Alexandria University, Alexandria, Egypt*
[2] *Institute of Basic and Applied Science, College of Engineering, Arab Academy for Science, Technology and Maritime Transport, Alexandria, Egypt*

**Abstract.** This study develops an analytical formulation to investigate the thermocapillary and photocapillary migration dynamics of a spherical fluid droplet suspended within a saturated, homogeneous, and isotropic porous matrix, assuming local thermal equilibrium. A uniform external thermal gradient, parallel to an adiabatic boundary, drives the migration. The analysis operates under low Péclet ($Pe \ll 1$) and Reynolds ($Re \ll 1$) numbers, implying negligible advective heat transport and inertial effects, respectively. Consequently, the thermal field is governed by Laplace's equation, internal droplet fluid motion by Stokes equations, and interstitial flow by the Brinkman equation. Analytical expressions for the droplet's translational velocities and associated hydrodynamic forces are derived, examining the influence of the Brinkman parameter ($\alpha$), thermal conductivity ratio ($k$), and viscosity ratio ($\sigma$) on droplet kinematics. Furthermore, the limiting Stokes (high permeability) and Darcy (low permeability) flow regimes are analyzed.

**2020 Mathematics Subject Classifications**: 76S05, 76D07, 76T30

**Key Words and Phrases**: Brinkman flow, Thermocapillary, Photocapillary, Spherical droplet

## 1. Introduction

The mobility of droplets and bubbles driven by gradients in interfacial tension—commonly referred to as thermocapillary or Marangoni migration—is a phenomenon of fundamental importance in several scientific and practical applications. Such interfacial tension gradients often occur from spatial changes in temperature or concentration, creating a tangential stress at the droplet surface that leads in directed motion [1]. Thermocapillary migration plays a crucial role in materials processing, microfluidics, environmental remediation, and increased oil recovery [2–5].

The standard theoretical foundation for thermocapillary migration was provided by Young et al. [6], who produced an analytical expression for the velocity of a spherical

---

[*] Corresponding author.

DOI: https://doi.org/10.29020/nybg.ejpam.v18i3.6505

*Email address:* `samar.mahrous@aast.edu` (S. A. Mahrous)

bubble or drop migrating in an unbounded fluid subject to a uniform temperature gradient. Assuming a creeping flow and negligible convective heat transfer, their model revealed that the migration velocity is proportional to the thermal gradient and the surface tension's temperature coefficient. Although immensely important, this concept applies exclusively to isolated drops in idealized situations.

In practical applications, migrating droplets often engage with adjacent interfaces, such as confining walls or other droplets, which considerably modify their movement. Over the past few decades, a vast variety of analytical and numerical investigations has addressed such confinement effects [7–11]. Meyyappan et al. [7] and Sadhal [12] examined the migration of gaseous bubbles near planar surfaces, utilizing spherical bipolar coordinates to elucidate quasi-steady dynamics. Meyyappan and Subramanian [13] expanded this concept to examine bubble migration parallel to a barrier, demonstrating a monotonic reduction in velocity relative to the unbounded scenario as the bubble neared the interface [14, 15].

Subsequent inquiries examined the thermocapillary movement of fluid droplets adjacent to planar surfaces. Barton and Subramanian [16] and Chen and Keh [17] expanded the analysis to liquid droplets, whereas Barton and Subramanian [18] offered experimental validation for droplets traveling perpendicular to a horizontal surface. Comparable theoretical findings were achieved through boundary collocation by Chang and Keh [19], and for spherical cavities by Lee and Keh [20, 21]. Asymptotic methods, including lubrication theory [22] and the method of reflections [23, 24], elucidated the impact of proximity to interfaces on droplet mobility.

Recently, sophisticated numerical methods have facilitated more profound inquiries. Choudhuri and Raja Sekhar [25] examined thermocapillary drift through decoupled solutions for thermal and momentum transfer. Chiu and Keh [26] examined droplet motion in cylindrical tubes, demonstrating that the droplet's velocity is influenced by both viscous drag and wall-induced alterations to thermal gradients. Chennuri and Prakash [27] investigated a concentric compound drop in arbitrary flow, developing closed-form formulas for migration velocity and hydrodynamic forces, while emphasizing the effects of Marangoni number and inner drop radius.

Although extensive research has been conducted on thermocapillary migration in transparent fluids, comparable phenomena in porous media have received comparatively scant attention. The interaction between interfacial thermal gradients and hydrodynamic resistance caused by the porous structure poses a distinct challenge in these environments. Although the Darcy and Darcy–Brinkman equations have been employed to predict flow in porous media [28], previous research has largely overlooked the influence of temperature-dependent surface tension in these systems.

This study examines the thermocapillary and photocapillary movement of a spherical fluid droplet within a Brinkman medium. Our objective is to comprehend how porous permeability influences both flow and heat fields, therefore affecting migration velocity. The Darcy–Brinkman model is adopted to bridge the classical Darcy flow regime (low permeability) with Stokes flow (high permeability), enabling direct comparison with existing clear-fluid results. To the best of our knowledge, this is one of the first analytical studies to consider thermocapillary (and photocapillary) effects in a Brinkman medium.

## 2. Modeling of Thermal Energy Transport Through a Porous Medium

In this section, we present the energy conservation equation to describe heat transfer within a porous medium based on the first law of thermodynamics. The porous medium is assumed to be homogeneous and isotropic. Let $T_s$ and $T_f$ denote the temperatures of the solid and fluid phases, respectively, with the assumption that there is thermal equilibrium between these two phases such that $T_s = T_f = T$. This assumption implies that at every point in the medium, the solid matrix and the interstitial fluid are at the same temperature. Furthermore, we neglect several effects to simplify the analysis of the current problem, including; heat generation due to radioactive decay, viscous dissipation, and work done by pressure changes. Additionally, the Péclet number of the fluid phase is assumed to be small, which implies that conductive heat transfer dominates over convective heat transfer. Under these assumptions, and considering a steady-state regime with no internal heat sources, the governing energy equation for the porous medium reduces to:

$$\nabla \cdot k_p \nabla T = 0, \tag{2.1}$$

where $k_p$ represents the effective thermal conductivity of the porous medium, defined as:

$$k_p = (1-\phi)k_s + \phi k_f, \tag{2.2}$$

here, $k_s$ and $k_f$ are the thermal conductivities of the solid and fluid phases, respectively, and $\phi$ is the porosity of the medium.

## 3. Thermocapillary Driven Migration of a Spherical Droplet Embedded in a Porous Medium

We examine a spherical droplet, denoted as $S_d$, with radius $a$ and thermal conductivity $k_d$, situated within an infinite porous medium having effective thermal conductivity $k_p$. Let $(r, \theta, \phi)$ represent a system of spherical coordinates with origin $O$ located at the center of the droplet $S_d$. The corresponding unit vectors in this coordinate system are $\vec{e}_r$, $\vec{e}_\theta$, and $\vec{e}_\phi$. At large distances from the droplet, the porous medium is subjected to a uniform and constant temperature gradient, denoted by $E_\infty$, directed parallel to the $z$-axis, as illustrated in Fig. 1. In the current formulation, we assume that all thermal properties of both the droplet and the porous medium are constant and do not vary with position or temperature. The problem is analyzed in two stages: first, we drive the temperature distribution fields within the droplet and the surrounding porous medium; and second, we develop the corresponding flow field induced by thermocapillary effects on the droplet and the Brinkman porous medium.

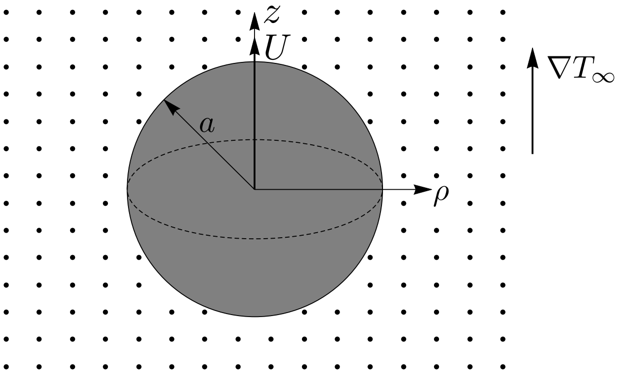

Figure 1: Geometrical sketch for a spherical droplet $S_d$ embedded in a porous medium.

### 3.1. Thermal Distributions of The Spherical Droplet and The Porous Medium

According to the assumptions stated earlier, the energy equation governing the temperature distribution $T_d(r, \theta)$ for the viscous fluid inside the spherical droplet, with thermal conductivity $k_d$, is given by the steady-state Laplace equation:

$$\nabla^2 T_d = 0, \quad r < a. \tag{3.1}$$

Similarly, for the porous medium surrounding the droplet with effective thermal conductivity $k_p$, the temperature distribution satisfies:

$$\nabla^2 T_p = 0, \quad r > a. \tag{3.2}$$

It should be noted that equations (3.1) and (3.2) omit the convective heat transfer term. This is justified under the assumption of low Reynolds number and small droplet size, where the fluid motion is slow and the corresponding Péclet number is small. In such regimes, heat conduction dominates over convection [29], allowing the convective effects to be neglected. However, if the Péclet number is of order 0.1 or higher, convective effects may become significant and should not be disregarded [30]. The boundary conditions at the droplet surface ($r = a$) require that both the temperature and the normal heat flux be continuous across the interface. Additionally, far from the droplet, the fluid temperature should approach the linear profile imposed in the ambient medium, while inside the droplet it remains finite. Now the boundary conditions are stated as:

$$\left.\begin{aligned} T_p &= T_d, \qquad r = a, \\ k_p \frac{\partial T_p}{\partial r} &= k_d \frac{\partial T_d}{\partial r}, \; r = a, \end{aligned}\right\} \tag{3.3}$$

$$T_d \text{ is finite, } r < a. \tag{3.4}$$

We place the origin of the coordinate system at the droplet center. A linear temperature field $T_\infty(z)$ is imposed in the far field of the surrounding fluid, described by:

$$T_\infty = T_0 + E_\infty z = T_0 + E_\infty r \cos\theta, \tag{3.5}$$

where $E_\infty$ is unvarying and $T_0$ is also a constant that represent the reference temperature at the droplet center. The capillary number $Ca$ is assumed to be small (that is, the surface tension dominates viscous forces), ensuring that the droplet maintains a spherical shape under thermocapillary migration. Solving the Laplace equations with the above boundary conditions yields the following expressions for the temperature distributions in the porous medium and inside the droplet:

$$T_p = T_0 + E_\infty \left[1 - \frac{k-1}{2+k}\left(\frac{a}{r}\right)^3\right] r\cos\theta, \tag{3.6}$$

$$T_d = T_0 + \frac{3E_\infty}{2+k} r\cos\theta, \tag{3.7}$$

where $k = k_d/k_p$ is the ratio of thermal conductivities of the droplet to the porous medium.

## 3.2. Fluid Flow Inside Both The Droplet and The Porous Medium in The Case of Thermocapillary Migration

The governing equations for the slow, steady, and incompressible flow of a viscous fluid through a porous medium are derived from the Brinkman model. This model is a modification of the classical Darcy's law and incorporates viscous shear effects by including a Laplacian term. Assuming the absence of body forces and negligible inertial effects (i.e., low Reynolds number flow), the equations simplify and can be written as:

$$\nabla \cdot \vec{q} = 0, \tag{3.8}$$

$$\widetilde{\mu}\nabla^2\vec{q} - \frac{\mu}{K}\vec{q} = \nabla P, \tag{3.9}$$

where $\vec{q}$ is the volume-averaged fluid velocity vector, $P$ denotes the pore-averaged pressure, $\mu$ is the dynamic viscosity of the fluid, and $K$ is the permeability of the porous medium. The term $\tilde{\mu}$ represents the effective viscosity, which accounts for both the fluid and the porous matrix interactions. These equations model the fluid dynamics inside the porous domain, where the Laplacian term $\left(\nabla^2\vec{q}\right)$ captures the internal viscous stresses, and the term $\left(\frac{\mu}{K}\vec{q}\right)$ models the Darcy drag due to the porous structure. The associated stress tensor $\Pi$ within the Brinkman framework is formulated as:

$$\Pi = -PI + 2\widetilde{\mu}\Delta, \tag{3.10}$$

where $I$ is the identity tensor and $\Delta$ is the rate-of-strain tensor given by:

$$\Delta = \tfrac{1}{2}\left(\nabla\vec{q} + (\nabla\vec{q})^T\right). \tag{3.11}$$

This formulation is particularly suitable for modeling flow at micro-scales, such as in thermophoretic or thermocapillary scenarios where the transport is driven by temperature gradients and the effects of convective inertia are neglected as in the current study. Let $U$

be the thermocapillary velocity of the droplet in the $z-$ direction to be determined. The motion is axisymmetric in which

$$\vec{q}(r,\theta) = q_r\vec{e_r} + q_\theta\vec{e_\theta}. \tag{3.12}$$

From the incompressibility equation (3.8), accordingly we obtain the velocity components $q_r$ and $q_\theta$ in terms of the Stokes' stream function $\psi$, as

$$q_r = -\frac{1}{r^2\sin\theta}\frac{\partial\psi}{\partial\theta}, \quad q_\theta = \frac{1}{r\sin\theta}\frac{\partial\psi}{\partial r}. \tag{3.13}$$

Substituting in the field equation (3.9), we obtain an equation satisfied by the stream function in a dimensionless form as:

$$E^2\big(E^2 - \alpha^2\big)\psi^{(p)} = 0, \quad r > 1, \tag{3.14}$$

where,

$$E^2 \equiv \frac{\partial^2}{\partial r^2} + \frac{1-\zeta^2}{r^2}\frac{\partial^2}{\partial\zeta^2}, \quad \zeta = \cos\theta, \quad \alpha = \sqrt{\frac{\mu a^2}{\widetilde{\mu}K}}.$$

The pressure within the porous medium, is given by integrating the following relations

$$\left.\begin{aligned} \frac{\partial P^{(p)}}{\partial r} &= -\frac{\widetilde{\mu}}{r^2\sin\theta}\frac{\partial}{\partial\theta}\big(E^2-\alpha^2\big)\psi^{(p)}, \\ \frac{\partial P^{(p)}}{\partial\theta} &= \frac{\widetilde{\mu}}{\sin\theta}\frac{\partial}{\partial r}\big(E^2-\alpha^2\big)\psi^{(p)}. \end{aligned}\right\} \tag{3.15}$$

Whereas, the vorticity vector is given by:

$$\vec{\omega}^p = \frac{\vec{e_\phi}}{2r\sin\theta}E^2\psi^{(p)}. \tag{3.16}$$

Now, inside the droplet, given the same conditions applied as the flow inside the porous medium, the governing equation would be the simplified Stokes equation, that is, by removing the Darcy's term from equation (3.9). Similarly, by incorporating the stream function $\psi^{(d)}$, the Stokes equation becomes:

$$E^4\psi^{(d)} = 0, \quad r < 1. \tag{3.17}$$

The porous stream function $\psi^{(p)}$ can be defined as $\psi^p = \psi_1^{(p)} + \psi_2^{(p)}$, where $E^2\psi_1^{(p)} = 0$ and $\big(E^2-\alpha^2\big)\psi_2^{(p)} = 0$, on that, equations (3.15) and (3.16) become

$$\frac{\partial P^{(p)}}{\partial r} = \frac{\widetilde{\mu}\alpha^2}{r^2\sin\theta}\frac{\partial\psi_1^{(p)}}{\partial\theta}, \quad \frac{\partial P^{(p)}}{\partial\theta} = -\frac{\widetilde{\mu}\alpha^2}{\sin\theta}\frac{\partial\psi_2^{(p)}}{\partial r}, \tag{3.18}$$

$$\omega^{(p)} = \frac{\alpha^2\psi_2^{(p)}}{2r\sin\theta}. \tag{3.19}$$

To complete the formulation of the present problem, the boundary conditions for the fluid velocity components along the droplet/porous interface must be specified. Here, we consider thermal capillarity along the surface of the interface at $r = 1$:

$$q_r^{(p)} = q_r^{(d)}, \tag{3.20}$$

$$q_\theta^{(p)} = q_\theta^{(d)}, \tag{3.21}$$

$$q_r^{(p)} = U \cos\theta, \tag{3.22}$$

$$\tau_{r\theta}^{(p)} - \tau_{r\theta}^{(d)} = -\left(\frac{\partial \gamma}{\partial T}\right)\frac{1}{r}\frac{\partial T_p}{\partial \theta}, \tag{3.23}$$

$$as\ r \to \infty, \quad \frac{\psi^{(p)}}{r^2} \to 0, \tag{3.24}$$

where $\gamma$ is the surface tension. The general solution of equation (3.17), that is bounded for $r \to 0$, is given by:

$$\psi^{(d)} = \left(A^{(d)} r^4 + C^{(d)} r^2\right) \sin^2\theta. \tag{3.25}$$

Also, the general solution of equation (3.14), that satisfy condition (3.24), is:

$$\psi^{(p)} = \left(\frac{A^{(p)}}{r} + B^{(p)}\left(\frac{1}{r} + \alpha\right) e^{-\alpha(r-1)}\right) \sin^2\theta. \tag{3.26}$$

Using (3.13), the components of the velocities of the flow through the porous medium and inside the droplet are stated below;
equation (3.13) and equation (3.25) give,

$$q_r^{(d)} = -2(A^{(d)} r^2 + C^{(d)}) \cos\theta, \tag{3.27}$$

$$q_\theta^{(d)} = (4A^{(d)} r^2 + 2C^{(d)}) \sin\theta. \tag{3.28}$$

equation (3.13) with (3.26) give,

$$q_r^{(p)} = -2\left(\frac{A^{(p)}}{r} + B^{(p)}\left(\frac{1}{r^3} + \frac{\alpha}{r^2}\right) e^{-\alpha(r-1)}\right) \cos\theta, \tag{3.29}$$

$$q_\theta^{(p)} = -\left(\frac{A^{(p)}}{r^3} + B^{(p)}\left(\frac{1}{r^3} + \frac{\alpha}{r^2} + \frac{\alpha^2}{r}\right) e^{-\alpha(r-1)}\right) \sin\theta. \tag{3.30}$$

The shear stress expression in terms of the velocity components, is given by:

$$\tau_{r\theta} = \mu\left[\frac{1}{r}\frac{\partial q_r}{\partial \theta} - \frac{q_\theta}{r} + \frac{\partial q_\theta}{\partial r}\right],$$

for the fluid droplet:

$$\tau_{r\theta}^{(d)} = \mu[6A^{(d)} r \sin\theta], \tag{3.31}$$

and for the porous medium:

$$\tau_{r\theta}^{(p)} = \widetilde{\mu}\left[\left(\frac{6A^{(p)}}{r^4} + B^{(p)}\left(\frac{6}{r^4} + \frac{6\alpha}{r^3} + \frac{3\alpha^2}{r^2} + \frac{\alpha^3}{r}\right)e^{-\alpha(r-1)}\right)\sin\theta\right]. \tag{3.32}$$

We have also,

$$\frac{1}{r}\frac{\partial T_p}{\partial \theta} = -\frac{3E_\infty}{2+k}. \tag{3.33}$$

Applying the boundary conditions (3.20)-(3.23), we obtain the following set of simultaneous equations for determining the unknown constants:

$$A^{(d)} - A^{(p)} + C^{(d)} - (1+\alpha)B^{(d)} = 0, \tag{3.34}$$

$$4A^{(d)} + A^{(p)} + 2C^{(d)} + (1+\alpha+\alpha^2)B^{(p)} = 0, \tag{3.35}$$

$$A^{(p)} + B^{(p)}(1+\alpha) = -\frac{U}{2}, \tag{3.36}$$

and

$$\widetilde{\mu}\left[\left(\frac{6A^{(p)}}{r^4} + B^{(p)}\left(\frac{6}{r^4} + \frac{6\alpha}{r^3} + \frac{3\alpha^2}{r^2} + \frac{\alpha^3}{r}\right)e^{-\alpha(r-1)}\right)\sin\theta\right] - \mu[6A^{(d)}r\sin\theta]$$
$$= -\left(\frac{\partial\gamma}{\partial T_d}\right)\left(\frac{-3E_\infty}{2+k}\sin\theta\right),$$

by simplifying the above equation, it becomes:

$$6A^{(p)} + (6+6\alpha+3\alpha^2+\alpha^3)B^{(p)} - 6\sigma A^{(d)} = \frac{3U^{(0)}}{2+k}, \tag{3.37}$$

where, $\sigma = \mu/\widetilde{\mu}$, and characteristic velocity $U^{(0)} = \beta E_\infty/\widetilde{\mu}$, $\beta$ is the constant $(-\partial\gamma/\partial T_d)$. Solving the above system we obtain,

$$A^{(p)} = -\left(U\frac{3(2+3\sigma)(1+\alpha) + 3(1+\sigma)\alpha^2 + \alpha^3}{2\big(3(1+\sigma)\alpha^2+\alpha^3\big)} + U^{(0)}\frac{6(1+\alpha)}{(2+k)\big(3(1+\sigma)\alpha^2+\alpha^3\big)}\right), \tag{3.38}$$

$$B^{(p)} = \tfrac{3}{2}U\frac{(3k+6)\sigma + 2k + 4}{\gamma_1} + U^{(0)}\frac{3}{\gamma_1}, \tag{3.39}$$

$$A^{(d)} = \tfrac{3}{4}U\frac{((1+\alpha)k + 2\alpha + 2)}{\gamma_2} - U^{(0)}\frac{3/2}{\gamma_2}, \tag{3.40}$$

$$C^{(d)} = -\tfrac{1}{4}U\frac{(6k+12)\sigma + (5\alpha+9)k + 10\alpha + 18}{\gamma_2} + U^{(0)}\frac{3/2}{\gamma_2}, \tag{3.41}$$

where,

$$\gamma_1 = \alpha^2\big((3k+6)\sigma + (\alpha+3)k + 2\alpha + 6\big),$$

and

$$\gamma_2 = (3k+6)\sigma + (\alpha+3)k + 2\alpha + 6.$$

### 3.3. Thermocapillary Velocity of The Droplet

The formula for the hydrodynamic drag force exerted by the porous medium on an axially symmetric droplet has the form

$$F = \widetilde{\mu}\alpha^2\left(UV_p + 4\pi \lim_{r\to\infty} \frac{r\psi^{(p)}}{\sin^2\theta}\right), \tag{3.42}$$

where $V_d$ is the volume of the droplet. The expression (3.42) can be derived in the same manner as that obtained by Lawrence and Weinbaum [31] for the axisymmetric motion of an oscillating body in a viscous fluid. Inserting the expression (3.26) for the stream function into (3.42) we obtain

$$F = \tfrac{4}{3}\pi\widetilde{\mu}\alpha^2(U + 3A^{(p)}). \tag{3.43}$$

Since the droplet is freely suspended in the porous medium, this force must vanish and equation (3.43) leads to $U + 3A^{(p)} = 0$, that gives the thermocapillary velocity of the spherical droplet in the porous medium as

$$U_T = \frac{18(\alpha+1)}{(2+k)\big(9(2+3\sigma)(1+\alpha) + 3(1+\sigma)\alpha^2 + \alpha^3\big)}U^{(0)}. \tag{3.44}$$

The normalized thermocapillary velocity is therefore

$$U_T^* = \frac{U_T}{U^{(0)}} = \frac{18(\alpha+1)}{(2+k)\big(9(2+3\sigma)(1+\alpha) + 3(1+\sigma)\alpha^2 + \alpha^3\big)}. \tag{3.45}$$

For a clear fluid, i.e. ($\alpha = 0$), we have:

$$U_0 = \frac{2U^{(0)}}{(2+k)(2+3\sigma)}. \tag{3.46}$$

This recovers the result of Luzhang et al. [1]. Knowing the thermocapillary velocity $U_T$ from equation (3.44) into equation (3.26), the porous stream function $\psi^{(p)}$ would be:

$$\begin{aligned}\psi^{(p)} = -\bigg[&\big(12(1+\alpha) - 6(1+\alpha r)e^{\alpha(1-r)}\big)U^{(0)} + \big((2+k)(6+9\sigma+\alpha(6\\ &+9\sigma+\alpha(3+3\alpha+3\sigma))) - 3(2+k)(1+\alpha r)(2+3\sigma)e^{\alpha(1-r)}\big)U\bigg]\frac{\sin^2\theta}{\delta_1},\end{aligned} \tag{3.47}$$

$$\delta_1 = 2(2+k)r\alpha^2(3+\alpha+3\sigma).$$

Also, the vorticity in equation (3.19) becomes:

$$\begin{aligned}\omega^{(p)} = -\bigg[&\big(12(1+\alpha) - 6(1+\alpha r)e^{\alpha(1-r)}\big)U^{(0)} + \big((2+k)(6+9\sigma+\alpha(6\\ &+9\sigma+\alpha(3+3\alpha+3\sigma))) - 3(2+k)(1+\alpha r)(2+3\sigma)e^{\alpha(1-r)}\big)U\bigg]\frac{\sin\theta}{\delta_2},\end{aligned} \tag{3.48}$$

$$\delta_2 = 2(2+k)r^2(3+\alpha+3\sigma).$$

### 3.4. Thermocapillary Force Acting on The Droplet

To find the thermocapillary force exerted on the droplet due to the prescribed temperature gradient $\nabla T_\infty$, we have to consider boundary condition (3.22) with vanishing particle velocity (i.e. $U = 0$) into the stream functions given by (3.25) and (3.26). Inserting (3.27)-(3.33) into the boundary conditions (3.20)-(3.23) (with $U = 0$), we get four simultaneous equations in the unknown constants $A^{(p)}$, $B^{(p)}$, $A^{(d)}$, and, $C^{(d)}$, the solution of which give $A^{(p)}$ in the following form,

$$A^{(p)} = \frac{3(\alpha+1)U^{(0)}}{\gamma_1}. \tag{3.49}$$

Again, by using formula (3.43) (with $U = 0$), the thermocapillary force acting on the droplet would be:

$$F_T = \frac{12\pi\widetilde{\mu}(\alpha+1)}{(3k+6)\sigma + (\alpha+3)k + 2\alpha + 6} U^{(0)}. \tag{3.50}$$

Now, the normalized thermocapillary force acting on the droplet is,

$$F_T^* = \frac{F_T}{12\pi\widetilde{\mu}U^{(0)}} = \frac{F_T}{12\pi E_\infty \beta} = \frac{\alpha+1}{(3k+6)\sigma + (\alpha+3)k + 2\alpha + 6}. \tag{3.51}$$

For very small $\alpha$, the asymptotic expansion of $F_T^*$ is given by:

$$F_T^* = \frac{1}{3(k+2)(\sigma+1)} \left[1 + \alpha\left(1-\delta\right) + \alpha^2\left(-\delta+\delta^2\right)\right] + \mathcal{O}(\alpha^3) \tag{3.52}$$

where, $\delta = 1/(3(\sigma+1))$. At ($\alpha = 0$) the force would correspond to a clear fluid and is given by:

$$F_0 = \frac{1}{3(k+2)(\sigma+1)}, \tag{3.53}$$

which recovers the result of Luzhang et al. [1]. It is obvious that in the presence of a porous structure, the normalized force is greater than the viscous counterpart.

## 4. Photocapillary Effects on the Spherical Droplet

In the context of photocapillary phenomena, the temperature distribution within the porous medium remains governed by the same formulation as in equation (3.2). However, the temperature inside the droplet—now absorbing electromagnetic radiation—is described by a new energy balance equation [32, 33]:

$$\nabla^2 \tilde{T}_d = -\frac{1}{k_d} Q(r,\zeta). \tag{4.1}$$

Here, $Q(r,\zeta)$ represents the volumetric energy generation [34] due to the absorption of incident radiation. For monochromatic radiation, the heat generation term is given by:

$$Q(r,\theta) = \frac{4\pi\nu\tilde{k}I}{\lambda} B(\xi,\zeta), \tag{4.2}$$

in this equation:

- $\nu$ and $\tilde{k}$ are the real and imaginary parts of the droplet's complex refractive index.
- $\lambda$ is the incident radiation wavelength.
- $B(\xi,\zeta) = \frac{|E(\xi,\zeta)|^2}{|E_0|^2}$ is a dimensionless electric field distribution where $E(\xi,\zeta)$ is the electric field of the particle and $E_0$ is the incident electric field strength.
- $\xi = \frac{r}{a}$, with $a$ being the droplet radius.

The boundary conditions remain similar to those discussed in the thermocapillary effects section, with a new outer condition as follows; matching the temperature and heat flux at the droplet interface ($\xi = 1$):

$$\tilde{T}_p = \tilde{T}_d, \quad k_p \frac{\partial \tilde{T}_p}{\partial \xi} = k_d \frac{\partial \tilde{T}_d}{\partial \xi}, \tag{4.3}$$

with

$$\tilde{T}_p \to T_\infty \quad \text{as} \quad r \to \infty. \tag{4.4}$$

We expand the internal temperature field as:

$$\tilde{T}_d = \frac{aI}{k_d} \sum_{n=0}^{\infty} F_n(\xi) P_n(\zeta). \tag{4.5}$$

Substituting into the heat equation from (4.1) yields:

$$\frac{d}{d\xi}\left(\xi^2 \frac{dF_n}{d\xi}\right) - n(n+1)F_n = -\frac{4\pi\nu\tilde{k}a}{\lambda}\xi^2 \Omega_n(\xi), \tag{4.6}$$

where,

$$\Omega_n(\xi) = \frac{1}{2}(2n+1)\int_{-1}^{1} B(\xi,\zeta)P_n(\zeta)\, d\zeta. \tag{4.7}$$

Solving via variation of parameters, the complete solution is given as:

$$F_n(\xi) = A_n^{(ph)}\xi^{-(n+1)} + B_n^{(ph)}\xi^n + S_n(\xi), \tag{4.8}$$

where, $A_n^{(ph)}$ and $B_n^{(ph)}$ are unknown constants to be determined, $S_n(\xi)$ is the particular solution of equation (4.6), that is given by:

$$S_n(\xi) = \frac{4\pi\nu\tilde{k}a^3}{\lambda(2n+1)}\left[\xi^n \int_{\xi}^{1} t^{-(n-1)}\Omega_n(t)dt + \xi^{-(n+1)}\int_0^{\xi} t^{n+2}\Omega_n(t)dt\right]. \tag{4.9}$$

Now the temperature profiles (as solutions of equations (3.2) and (4.1)) are as follows:

$$\tilde{T}_p = T_\infty + \frac{aI}{k}\sum_{n=0}^{\infty} B_n^{(ph)}\xi^n P_n(\zeta), \tag{4.10}$$

$$\tilde{T}_d = T_\infty + \frac{aI}{k}\sum_{n=0}^{\infty}(A_n^{(ph)}\xi^{-(n+1)} + S_n(\xi))P_n(\zeta). \tag{4.11}$$

Applying the boundary conditions at the droplet interface (4.3), the unknowns $A_n^{(ph)}$ and $B_n^{(ph)}$ are found to be:

$$A_n^{(ph)} = \frac{nS_n(1) - S_n'(1)}{nk+n+1}, \quad B_n^{(ph)} = \frac{-(n+1)S_n(1) + kS_n'(1)}{nk+n+1}, \tag{4.12}$$

where, $S_n' = dS_n/d\xi$ and $k = k_d/k_p$. The first term (at $n = 1$) in the series of the temperature profile at equation (4.11) would give $A_1^{(ph)}$ as:

$$A_1^{(ph)} = \frac{J_1}{k+2}, \tag{4.13}$$

where,

$$J_1 = S_1(1) - S_1'(1) = \frac{3\pi\nu\tilde{k}a}{\lambda}\int_0^1\int_0^\pi \xi^3 B(\xi,\theta)d\theta d\xi. \tag{4.14}$$

### 4.1. Fluid Flow Equations in Photocapillary Regime

We now repeat the same procedure as outlined in section (3.2), which encompasses applying the same boundary conditions. However, we replace every occurrence of $\psi^{(d)}$ with $\tilde{\psi}^{(d)}$, and every $\psi^{(p)}$ with $\tilde{\psi}^{(p)}$, this yields

$$\tilde{\psi}^{(d)} = \left(\tilde{A}^{(d)}r^4 + \tilde{C}^{(d)}r^2\right)\sin^2\theta, \tag{4.15}$$

$$\tilde{\psi}^{(p)} = \left(\frac{\tilde{A}^{(p)}}{r} + \tilde{B}^{(p)}\left(\frac{1}{r} + \alpha\right)e^{-\alpha(r-1)}\right)\sin^2\theta. \tag{4.16}$$

To determine the unknowns $\tilde{A}^{(d)}$, $\tilde{C}^{(d)}$, $\tilde{A}^{(p)}$, and $\tilde{B}^{(p)}$, we apply the boundary conditions (3.20)-(3.23) using the updated thermal distribution results for the photocapillary case. This leads to the following system of four simultaneous equations:

$$\tilde{A}^{(d)} - \tilde{A}^{(p)} + \tilde{C}^{(d)} - \tilde{B}^{(p)}(1+\alpha) = 0, \tag{4.17}$$

$$4\tilde{A}^{(d)} + \tilde{A}^{(p)} + 2\tilde{C}^{(d)} + \tilde{B}^{(p)}(1+\alpha+\alpha^2) = 0, \tag{4.18}$$

$$\tilde{A}^{(p)} + \tilde{B}^{(p)}(1+\alpha) = -\frac{U}{2}, \tag{4.19}$$

and,

$$\tilde{\mu}\left[\left(\frac{6\tilde{A}^{(p)}}{r^4} + \tilde{B}^{(p)}\left(\frac{6}{r^4} + \frac{6\alpha}{r^3} + \frac{3\alpha^2}{r^2} + \frac{\alpha^3}{r}\right)e^{-\alpha(r-1)}\right)\sin\theta\right] - \mu\left[6\tilde{A}^{(d)}r\sin\theta\right] = -\left(\frac{\partial\gamma}{\partial T}\right)\frac{1}{r}\frac{\partial\tilde{T}_p}{\partial\theta},$$

implying the following:

$$\frac{1}{r}\frac{\partial \tilde{T}_p}{\partial \theta} = \frac{IJ_1 \sin\theta}{k(k+2)\xi^3},$$

the fourth equation becomes:

$$6\tilde{A}^{(p)} + \tilde{B}^{(p)}(6 + 6\alpha + 3\alpha^2 + \alpha^3) - 6\sigma\tilde{A}^{(d)} = \frac{U_{Ph}^{(0)} IJ_1}{k(k+2)}, \tag{4.20}$$

where $\sigma = \mu/\widetilde{\mu}$, and characteristic velocity $U_{Ph}^{(0)} = \frac{1}{\tilde{\mu}}\left(\partial\gamma/\partial T\right)$. Now, we proceed to solving this linear system of equations to determine the unknowns, resulting the following expressions:

$$\begin{aligned}\tilde{A}^{(p)} = &-\frac{1}{2}U\left(k^2+2k\right)\alpha^3 \\ &+\frac{((3k^2+6k)(\sigma+1))\alpha^2 + ((9\sigma+6)k^2 + (18\sigma+12)k)(\alpha+1)}{\gamma_3} - \frac{1}{2}U_{Ph}^{(0)}\frac{2IJ_1(\alpha+1)}{\gamma_3},\end{aligned} \tag{4.21}$$

$$\tilde{B}^{(p)} = \frac{3}{2}U\frac{k^2(3\sigma+2) + 2k(3\sigma+2)}{\gamma_3} + U_{Ph}^{(0)}\frac{IJ_1}{\gamma_3}, \tag{4.22}$$

$$\tilde{A}^{(d)} = \frac{3}{4}U\frac{(\alpha+1)k^2 + 3(\alpha+1)k}{\gamma_4} - \frac{1}{2}U_{Ph}^{(0)}\frac{IJ_1}{\gamma_4}, \tag{4.23}$$

$$\tilde{C}^{(d)} = -\frac{1}{4}U\frac{(5k^2+10k)\alpha + 6\sigma k^2 + 9k^2 + 12\sigma k + 18k}{\gamma_4} + \frac{1}{2}U_{Ph}^{(0)}\frac{IJ_1}{\gamma_4}, \tag{4.24}$$

where,

$$\gamma_3 = \alpha^2 k(\alpha(k+2) + 3k(\sigma+1) + 6(\sigma+1)),$$
$$\gamma_4 = k(\alpha(k+2) + 3k(\sigma+1) + 6(\sigma+1)).$$

## 4.2. Photocapillary Velocity of The Droplet

Again, we repeat the same procedure described in Section (3.3) to derive the following relation: $U + 3\tilde{A}^{(p)} = 0$. From this, we obtain the expression for the photocapillary velocity as:

$$U_{Ph} = \frac{6IJ_1(1+\alpha)}{\left(\alpha^3 + 3\alpha^2(\sigma+1) + 9(\alpha+1)(3\sigma+2)\right)k(k+2)}U_{Ph}^{(0)}, \tag{4.25}$$

The normalized photocapillary velocity is then given by:

$$U_{Ph}^{*} = \frac{U_{Ph}}{IJ_1 U_{Ph}^{(0)}} = \frac{6(1+\alpha)}{\left(\alpha^3 + 3\alpha^2(\sigma+1) + 9(\alpha+1)(3\sigma+2)\right)k(k+2)}. \tag{4.26}$$

For a clear fluid ($\alpha = 0$), this simplifies to:

$$U_0^{(Ph)} = \frac{6IJ_1 U_{Ph}^{(0)}}{(27\sigma+18)k(k+2)}. \tag{4.27}$$

### 4.3. Photocapillary Force Acting on The Droplet

To determine the photocapillary force, we follow the same steps as in Section (3.4). We assume that the particle velocity vanishes (i.e., $U = 0$) in the boundary condition (3.22), hence we solve equations (4.17)–(4.20) under this new condition. Consequently, we obtain $\tilde{A}^{(p)}$ in the form:

$$\tilde{A}^{(p)} = \frac{I J_1 (1+\alpha)}{\gamma_3} U_{Ph}^{(0)}. \tag{4.28}$$

Inserting ($U = 0$) into equation (3.43), the resulting photocapillary force is given by:

$$F_{Ph} = \frac{4 I J_1 (1+\alpha)}{\gamma_4} U_{Ph}^{(0)}. \tag{4.29}$$

And the normalized photocapillary force is simply:

$$F_{Ph}^{*} = \frac{1+\alpha}{\gamma_4}. \tag{4.30}$$

## 5. Results and discussion

### 5.1. Thermocapillary

In this section, we present the results of the normalized thermocapillary velocity $U_T^*$ given by (3.45), and the normalized thermocapillary force $F_T^*$ given by (3.51) of a spherical droplet embedded in a porous medium. The parameters of the problem are as follows:

1. The permeability of the porous medium that characterize the nature of the porous medium, $\alpha = \sqrt{\mu a^2 / \widetilde{\mu} K}$. Values of $\alpha << 1$ means high permeability medium, that is $K >> 1$, with $\alpha = 0$ representing a viscous clear fluid, and $\alpha >> 1$ reduces the medium to a Darcian medium of low permeability $K << 1$.

2. The viscosity ratio $\sigma = \mu / \widetilde{\mu}$, which represents the ratio between the viscosity of the fluid inside the droplet and the effective viscosity of the porous medium, $0 \leq \sigma < \infty$. The value $\sigma = 0$ represents a bubble embedded in a porous medium, while $\sigma \to \infty$ represents a rigid particle.

3. The conductivity ratio $k = k_d / k_p$, which represents the ratio between the thermal conductivity of the fluid inside the droplet and the overall thermal conductivity of the porous medium. Note that the value of $k = 0$, which does not exist in practice, is covered in our graphs for comparison purposes, despite its non-existence in practice.

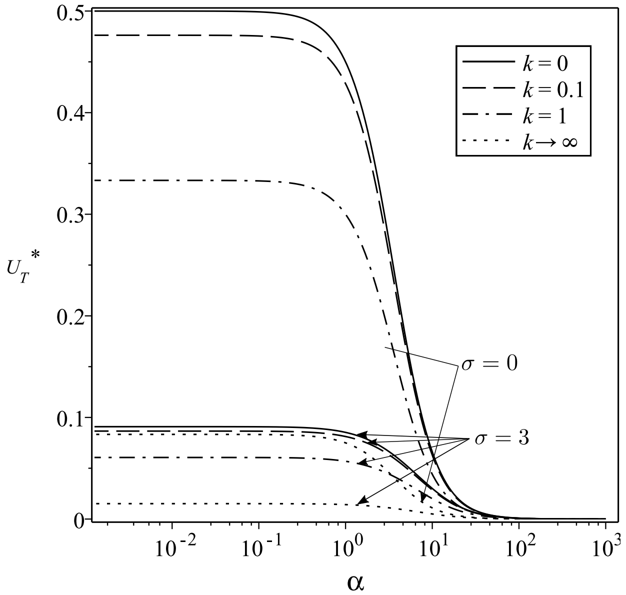

Figure 2: Normalized Thermocapillary velocity $U_T^*$ versus permeability parameter $\alpha$ for different values of thermal conductivity ratio $k$ at specific values of viscosity ratio($\sigma = 0$ , $\sigma = 3$).

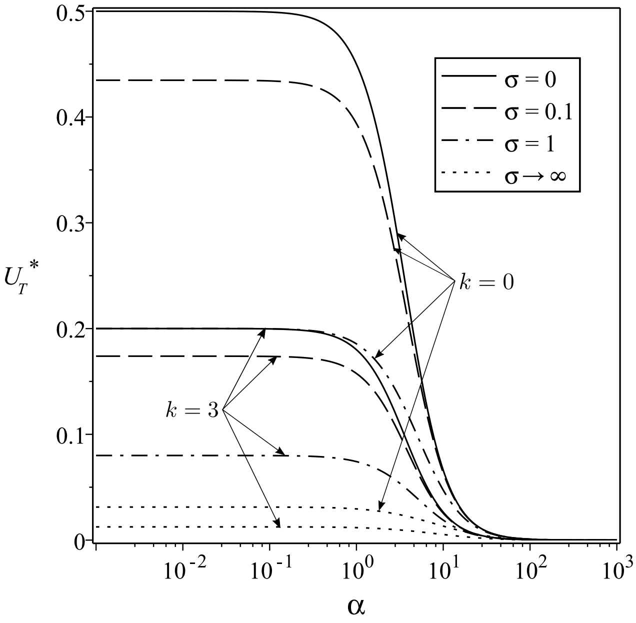

Figure 3: Normalized Thermocapillary velocity $U_T^*$ versus permeability parameter $\alpha$ for different values of viscosity ratio $\sigma$ at specific values thermal conductivity ratio ($k = 0$ , $k = 3$).

Figures 2 and 3 show the plots of $U_T^*$ against the permeability parameter characterizing the porous medium for various values of viscosity ratio $\sigma$, and the thermal conductivity ratio $k$. As depicted in Fig. 2 and Fig. 3, the presented results reveal a clear dependence of the dimensionless thermocapillary velocity $U_T^*$ on the porous medium's permeability $\alpha$, the droplet-to-medium viscosity ratio $\sigma$, and the droplet-to-medium thermal conductivity ratio $k$. A consistent attenuation of $U_T^*$ is observed with increasing permeability parameter $\alpha$, signifying the escalating hydrodynamic drag imposed by the porous matrix; this effect is most pronounced as $\alpha$ transitions from values near unity to higher values, culminating in negligible velocity in the Darcy limit ($\alpha >> 1$) where matrix resistance dominates, contrasting with maximal velocity in the Stokes limit ($\alpha = 0$) where such resistance is minimal. The physics underlying this trend is the increased energy dissipation due to the solid matrix obstructing flow. Furthermore, for fixed $\alpha$ and $\sigma$, an increase in the thermal conductivity ratio $k$ leads to a reduction in $U_T^*$. This is attributable to the droplet becoming more thermally conductive relative to the surrounding medium, which tends to homogenize the temperature across the droplet's surface, thereby diminishing the interfacial temperature gradients that are crucial for generating the Marangoni stresses responsible for migration. Conversely, at constant $\alpha$ and $k$, $U_T^*$ increases as the viscosity ratio $\sigma$ decreases (i.e., the droplet becomes less viscous relative to the external fluid). Reduced internal droplet viscosity promotes stronger internal circulation and surface mobility due to interfacial thermocapillary stresses, leading to a higher overall translational velocity. These interconnected influences highlight how the balance between the thermocapillary driving force, shaped by thermal properties, and the resistive forces, governed by both fluid viscosities and the porous matrix structure, dictates the droplet's migratory behavior.

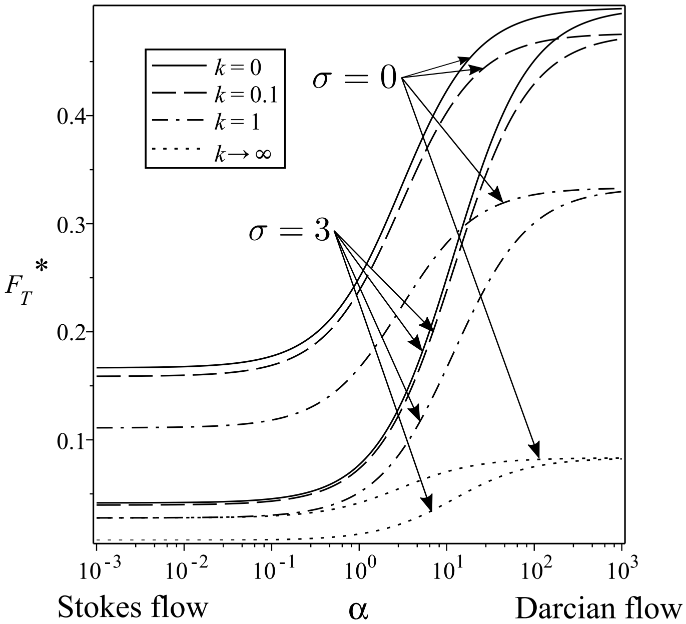

Figure 4: Normalized Thermocapillary Force $F_T^*$ versus permeability parameter $\alpha$ for different values of thermal conductivity ratio $k$ at specific values viscosity ratio ($\sigma = 0$ , $\sigma = 3$).

Figures 4 and 5 show the plots of the non-dimensional thermocapillary force $F_T^*$ against the permeability parameter $\alpha$ for various values of the viscosity ratio $\sigma$, and the thermal conductivity ratio $k$. The observed behavior of the non-dimensional thermocapillary force $F_T^*$ highlights the crucial interplay between internal fluid dynamics, interfacial phenomena, and overall droplet propulsion. $F_T^*$ increases monotonically with the permeability parameter $\alpha$ because higher permeability signifies reduced internal resistance to flow, leading to pronounced internal circulation and superior surface mobility, thereby enhancing the net propulsive force. Consequently, $F_T^*$ is minimized as $\alpha$ approaches zero, where the droplet behaves akin to a rigid particle with suppressed internal convection, and its asymptotes to a constant value as $\alpha$ approaches infinity, indicating that internal permeability is no longer the limiting factor and $F_T^*$ becomes governed by the magnitude of the interfacial temperature gradient (influenced by thermal conductivity ratio, $k$) and external fluid properties. Furthermore, for any given $\alpha$ and $k$, $F_T^*$ increases with a decreasing viscosity ratio $\sigma$, as lower internal viscosity reduces internal viscous dissipation, enabling the Marangoni stresses to more efficiently convert thermal energy into kinetic energy of internal and surface flows, thus augmenting the overall thermocapillary force.

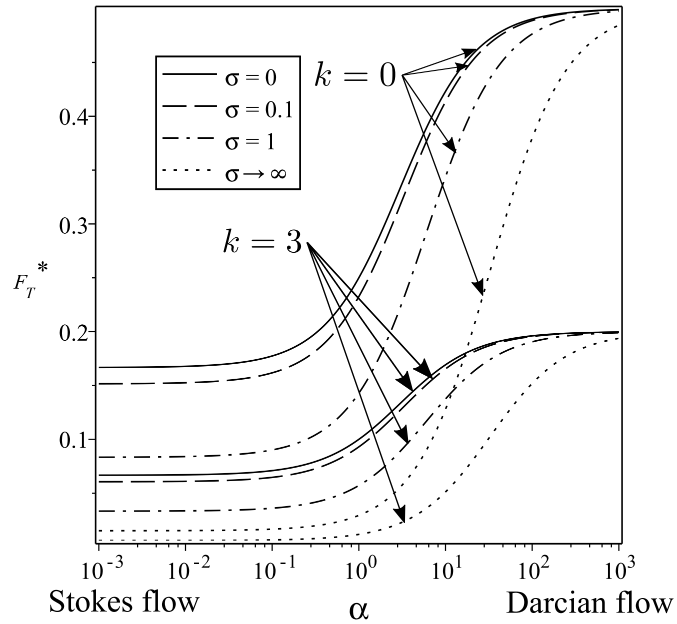

Figure 5: Normalized Thermocapillary force $F_T^*$ versus permeability parameter $\alpha$ for different values of viscosity ratio $\sigma$ at specific values thermal conductivity ratio ($k = 0$ , $k = 3$).

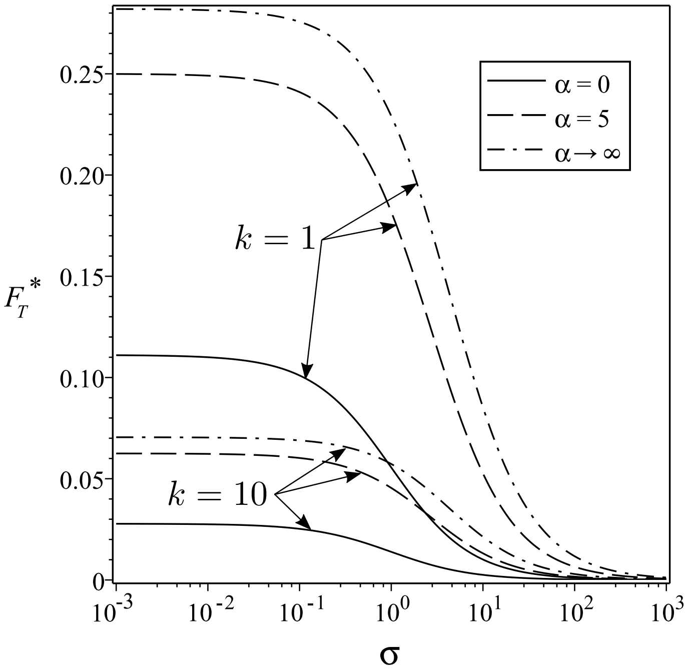

Figure 6: Normalized Thermocapillary force $F_T^*$ versus viscosity ratio $\sigma$ for different values of permeability parameter $\alpha$ at specific values of thermal conductivity ratio $k$ at ($k = 1$ , $k = 10$) .

The inverse relationship between the non-dimensional thermocapillary force $F_T^*$ and the viscosity ratio $\sigma$, as depicted in Fig. 6, is primarily attributable to the augmented internal hydrodynamic resistance within the droplet. An elevated $\sigma$, corresponding to an increased internal droplet viscosity, intensifies the viscous dissipation of mechanical energy derived from the temperature-gradient-induced Marangoni stresses at the interface. This increased internal dissipation not only impedes the establishment of robust internal convective flows, but also diminishes the droplet's surface mobility. Given that the net thermocapillary force is a manifestation of the efficient conversion of these interfacial stresses into coherent internal and surface kinematics, an elevated internal viscosity inherently diminishes the efficiency of converting interfacial energy into directed motion, leading to an attenuated propulsive force irrespective of the specific values of the thermal conductivity ratio $k$ or permeability $\alpha$.

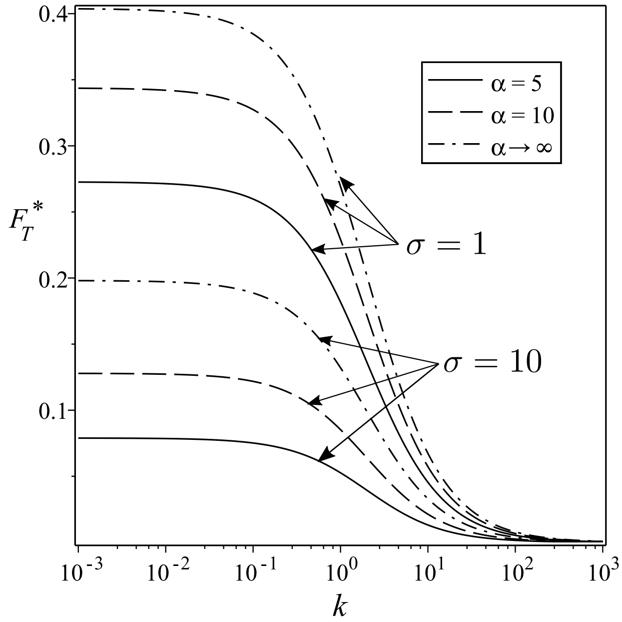

Figure 7: Normalized Thermocapillary force $F_T^*$ versus thermal conductivity ratio $k$ for different values of permeability parameter $\alpha$ at specific values of viscosity ratio $\sigma$ at ($\sigma = 1$ , $\sigma = 10$) .

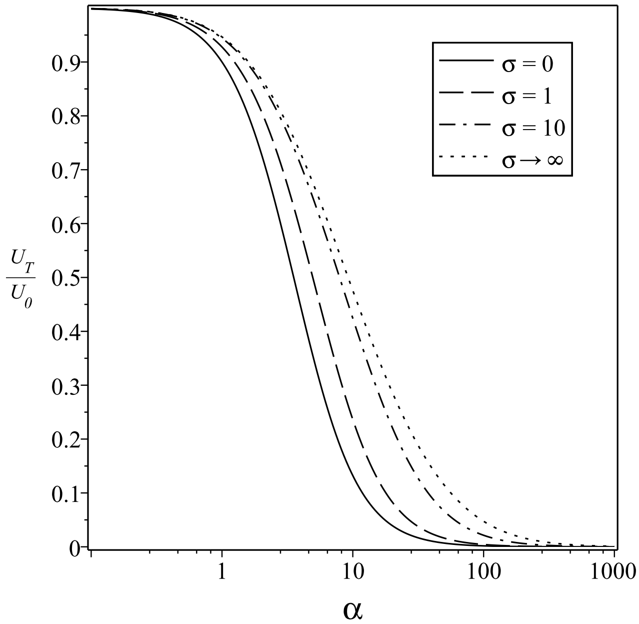

Figure 8: $U_T/U_0$ versus permeability parameter $\alpha$ for different values of viscosity ratio $\sigma$.

The observed dependencies of the non-dimensional thermocapillary force $F_T^*$ and the normalized translational velocity $U_T/U_0$ on the thermal conductivity ratio $k$, permeability parameter $\alpha$, and viscosity ratio $\sigma$, as illustrated in Figures 7, 8, and 9, provide critical insights into the physics governing thermocapillary migration within a porous medium, which align broadly with and extend established principles of thermocapillary migration and droplet dynamics in complex environments. Specifically, Fig. 7 reveals that $F_T^*$ decreases monotonically with an increasing thermal conductivity ratio $k$. This phenomenon arises because a higher $k$ implies that the droplet is more thermally conductive relative to its surroundings. Consequently, heat diffuses more readily through the droplet bulk, which can lead to a homogenization of the droplet's internal temperature and thereby reduce the magnitude of the temperature gradient sustained along its interface. A diminished interfacial temperature gradient directly translates to weaker Marangoni stresses, which are the driving mechanism for thermocapillary motion, thus resulting in a lower propulsive force and velocity, which is consistent with foundational theories [4, 6].

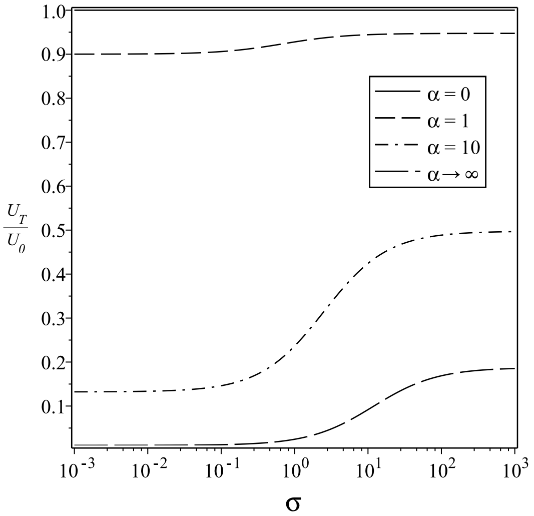

Figure 9: $U_T/U_0$ versus viscosity ratio $\sigma$ for different values of permeability parameter $\alpha$ .

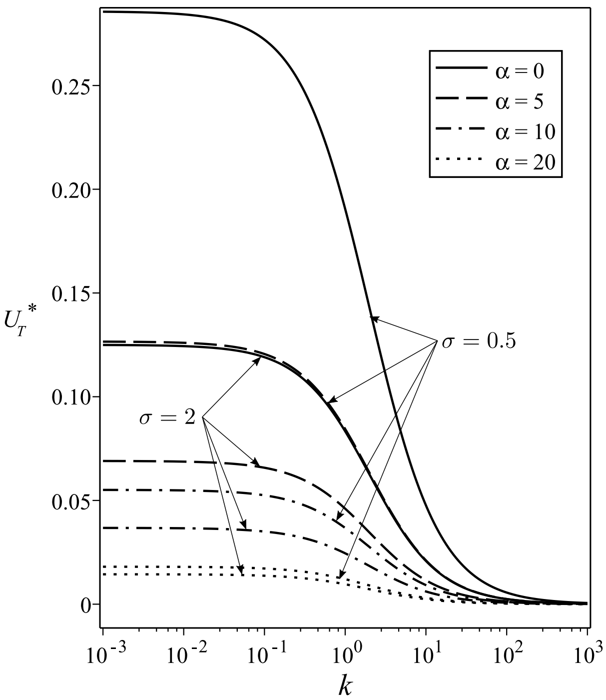

Figure 10: Normalized thermocapillary velocity $U_T^*$ versus thermal conductivity ratio $k$ for different values of permeability parameter $\alpha$ at specific values of viscosity ratio($\sigma = 0.5$ , $\sigma = 2$).

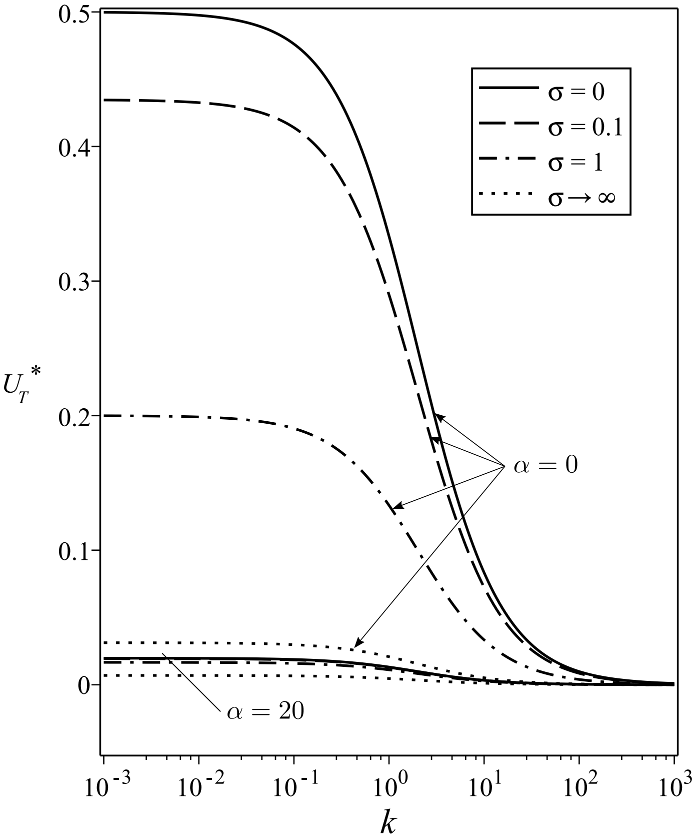

Figure 11: Normalized thermocapillary velocity $U_T^*$ versus thermal conductivity ratio $k$ for different values of viscosity ratio $\sigma$ at specific values of permeability parameter($\alpha = 0$ , $\alpha = 20$).

Furthermore, the corresponding trends observed for $U_T/U_0$ with respect to the permeability parameter $\alpha$, Fig. 8 and the viscosity ratio $\sigma$, Fig. 9, mirroring the behavior of $F_T^*$, underscore the direct translation of induced force into droplet kinematics. An increase in $\alpha$, signifying reduced internal resistance to flow or enhanced ease of navigating the porous matrix, facilitates more powerful internal circulation and droplet deformation in response to Marangoni stresses, thereby augmenting $U_T/U_0$. The intriguing limit where $\lim_{\alpha\to 0} U_T/U_0 = 1$ indicates that as the droplet's internal resistance to deformation becomes exceedingly high (or its ability to effectively utilize internal flows to navigate the pore space diminishes), its normalized velocity in the porous medium approaches that observed in an unconfined, clear viscous fluid $U_0$; this suggests that $U_0$ acts as a baseline for a droplet whose motion is primarily limited by its intrinsic properties rather than the specific additional impedance of the porous structure under such limiting conditions. Finally, the inverse relationship between $F_T^*$ and $U_T/U_0$ and the viscosity ratio $\sigma$ is well-documented [6, 35]; higher internal droplet viscosity leads to increased internal viscous dissipation, damping both internal convective flows and surface mobility, thereby inherently limiting the efficiency with which interfacial thermal energy is converted into kinetic energy for propulsion. These collective findings underscore the intricate coupling between interfacial thermophysics, internal droplet fluid mechanics, and the hydrodynamics imposed by the porous medium in dictating thermocapillary-driven transport.

Fig. 10 illustrates the dependence of the normalized thermocapillary velocity $U_T^*$ on the thermal conductivity ratio $k$ for varying permeability parameter $\alpha$ at specific values of viscosity ratio ($\sigma = 0.5,\ \sigma = 2$). The parameter $U_T^*$ consistently exhibits a characteristic non-linear decrease as $k$ increases, featuring an initial phase of relatively stable values at low thermal conductivity ratio ($k < 10^{-1}$) where the droplet effectively sustains an external temperature gradient. This is followed by a significant reduction in $U_T^*$ as $k$ increases ($10^{-1} < k < 10^2$) due to enhanced internal thermal homogenization, with $U_T^*$ ultimately approaching zero at high thermal conductivity ratio ($k > 10^2$). The viscosity ratio markedly influences velocity magnitude: ($\sigma = 0.5$ - less viscous droplet) results in substantially higher $U_T^*$ values (reaching initial stable values near 0.28 for $\alpha = 0$) compared to ($\sigma = 2$ more viscous droplet, with initial stable values near 0.125 for $\alpha = 0$), a difference attributed to reduced viscous resistance at lower $\sigma$. Interestingly, the permeability parameter $\alpha$ demonstrates a varied impact depending on $\sigma$. For ($\sigma = 0.5$), $U_T^*$ is largely independent of $\alpha$, while for ($\sigma = 2$), increasing $\alpha$ from 0 to 20 systematically lowers $U_T^*$. This suggests that for more viscous droplets, higher permeability may induce internal flows that either disrupt the externally imposed interfacial temperature gradient or enhance internal thermal equilibration, thereby diminishing thermocapillary propulsion.

Fig. 11 shows the normalized thermocapillary velocity, $U_T^*$, as a function of the thermal conductivity ratio, k, for varying viscosity ratios ($\sigma = 0,\ 0.1\ ,1$, and $\sigma \to \infty$) at two distinct levels of the permeability parameter: ($\alpha = 0$ impermeable droplet, upper set of curves) and ($\alpha = 20$ highly permeable droplet, lower set of curves). A consistent trend observed across all conditions is the decrease of $U_T^*$ with increasing $k$, transitioning from an initial region where $U_T^*$ exhibits near-constant values at low thermal conductivity ratio ($k < 10^{-1}$) to near-zero values at high thermal conductivity ratio ($k > 10^2$). This general behavior reflects the shift from a scenario where the droplet effectively sustains an interfacial temperature gradient (low $k$) to one where enhanced internal thermal homogenization diminishes this gradient (high $k$). For an impermeable droplet ($\alpha = 0$, upper curves), the viscosity ratio $\sigma$ exerts a pronounced and systematic influence. $U_T^*$ is maximized for an inviscid droplet ($\sigma = 0$), reaching a near-constant value of approximately 0.5 in the low $k$ region. As $\sigma$ increases to 0.1 and then to 1, this near-constant velocity progressively decreases to around 0.43 and 0.2, respectively. In the limit of an infinitely viscous droplet ($\sigma \to \infty$, effectively a rigid particle), $U_T^*$ reaches its minimum for the ($\alpha = 0$) case. This monotonic decrease in $U_T^*$ with increasing $\sigma$ is due to greater internal viscous dissipation, which increasingly impedes the internal fluid circulation driven by Marangoni stresses, thereby reducing the overall translational velocity. A striking observation is the dominant effect of high permeability when ($\alpha = 20$ - lower curves). In this regime, $U_T^*$ is extremely attenuated across all investigated viscosity ratios, with values consistently remaining very low. Furthermore, the sensitivity of $U_T^*$ to the viscosity ratio $\sigma$ is substantially diminished when permeability is high; the curves for different $\sigma$ values at ($\alpha = 20$) are closely grouped. This indicates that high permeability facilitates such efficient internal thermal equilibration likely through enhanced internal advective heat transfer pathways enabled by the permeable structure that it effectively short-circuits the externally imposed thermal gradient. Consequently, the thermocapillary driving force is significantly reduced, irrespective of the droplet's internal viscosity.

Fig. 12 shows the streamlines of the two flows under study, the flow through the porous medium outside form the droplet ($r > a$) and the flow within the droplet itself ($r < a$). The (a), (b) and (c) figures show the variations in the streamlines for both regions with different values of the porosity parameter $\alpha$, the viscosity ratio $\sigma$ and the conductivity ratio $k$, while the last figure (d) show the case of a solid particle by employing the limiting case of $\sigma$ reaching infinity.

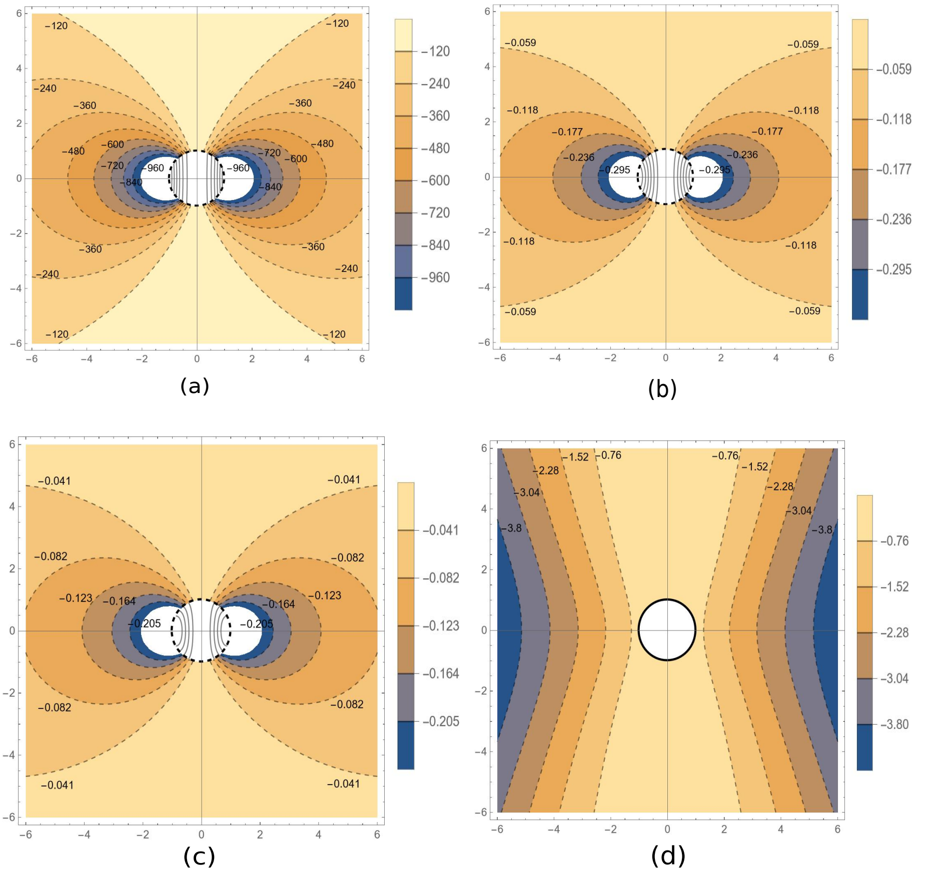

(a) (b) (c) (d)

Figure 12: The streamline function is scaled with respect to $Ua^2$ for translational motion: $\psi^{(i)}/Ua^2 = C_1,\ i = d, p$, where $C_1$ is a constant. Each contour is found by assigning a specific value to the constant $C_1$, with (a) $\alpha \to 0,\ \sigma = 0.5,\ k = 1$, (b) $\alpha = 5,\ \sigma = 1,\ k = 0.155$, (c) $\alpha \to \infty,\ \sigma = 3,\ k = 2$, (d) $\alpha \to 0,\ \sigma \to \infty,\ k = 2$ (Solid Particle).

## 5.2. Photocapillary

The investigation focuses on the non-dimensional photocapillary velocity $U^*_{Ph}$ and force $F^*_{Ph}$ for a spherical droplet within a porous medium, as defined by expressions (4.26) and (4.30) respectively. The dynamics are primarily governed by the permeability parameter ($\alpha = \sqrt{\mu a^2/\widetilde{\mu} K}$), which quantifies the porous medium's resistance to flow, the thermal conductivity ratio ($k = k_d/k_p$) between the droplet and the surrounding medium, and the viscosity ratio ($\sigma = \mu/\widetilde{\mu}$) between the droplet and the surrounding medium.

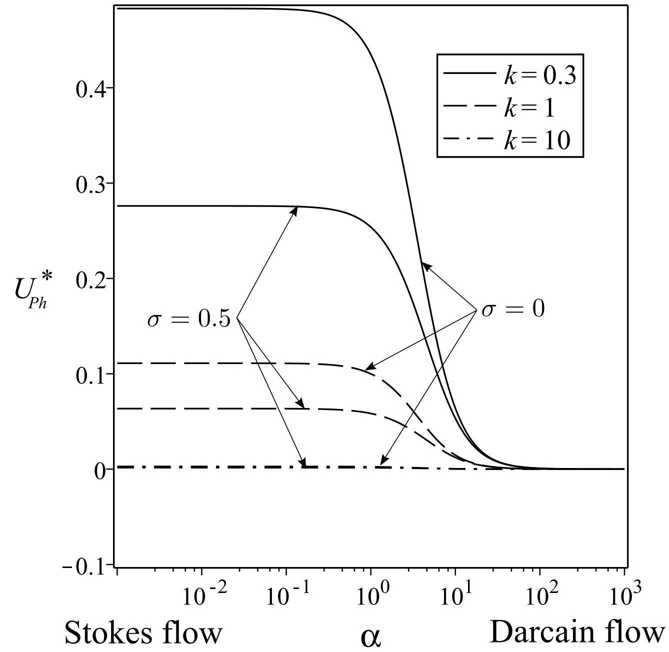

Figure 13: Normalized photocapillary velocity $U^*_{Ph}$ versus permeability parameter $\alpha$ for different values of thermal conductivity ratio $k$ at specific values of viscosity ratio($\sigma = 0$ , $\sigma = 0.5$).

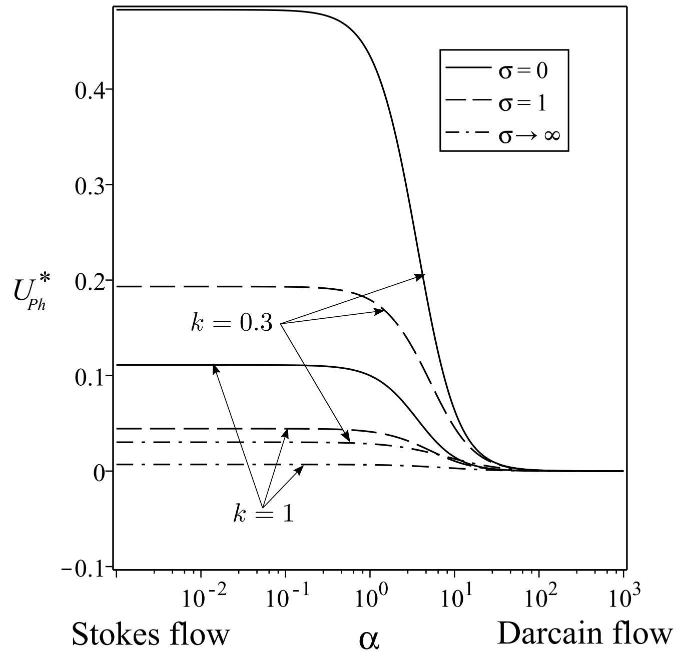

Figure 14: Normalized photocapillary velocity $U^*_{Ph}$ versus permeability parameter $\alpha$ for different values of viscosity ratio $\sigma$ at specific values thermal conductivity ratio ($k = 1$ , $k = 0.3$).

Figures 13 and 14 graphically depict how the thermocapillary velocity changes in response to variations in the permeability parameter. These illustrations further explore this relationship under several different conditions of thermal conductivity ratio and viscosity ratio. These figures show that $U^*_{Ph}$ generally decreases as $\alpha$ increases, across the entire range of thermal conductivity and viscosity ratios studied. In the Stokes limit ($\alpha = 0$), where the porous medium's influence is negligible, $U^*_{Ph}$ reaches its maximum value. This observation is consistent with classical analyses of thermocapillary migration in unbounded fluids, such as the seminal work by Young [6], where motion is driven by Marangoni stresses unimpeded by a porous matrix. For small permeability parameters ($\alpha < 1$), $U^*_{Ph}$ demonstrates a pronounced insensitivity, maintaining a relatively constant value. This regime signifies that the porous structure offers minimal resistance to the droplet's motion, mirroring the fluid dynamics within a highly permeable or sparsely constituted porous system. A sharp decline in $U^*_{Ph}$ is observed in the transitional regime ($1 < \alpha < 100$), indicating a significant increase in Darcy drag exerted by the porous medium. This behavior is analogous to the transition from Stokes flow to Darcy flow for rigid particles, though modified by the internal circulation and deformable interface of the droplet [36]. Finally, in the Darcian limit ($\alpha > 100$), where the porous medium's resistance dominates, the photocapillary velocity effectively vanishes. This is expected, as the pressure drop required to drive flow through a dense porous medium at a given velocity scales with decreasing permeability (increasing $\alpha$). Figures 10 and 11 also demonstrate that for a fixed $\alpha$, $U^*_{Ph}$ increases with a decrease in both the thermal conductivity ratio $k$ and the viscosity ratio $\sigma$. A lower $k$ (e.g., droplet less conductive than the medium, or medium more conductive than the droplet) can lead to steeper interfacial temperature gradients, enhancing the Marangoni effect. A lower $\sigma$ (droplet less viscous than the surrounding fluid) allows for more strong internal circulation within the droplet in response to surface tension gradients, translating to a higher translational velocity [6, 37].

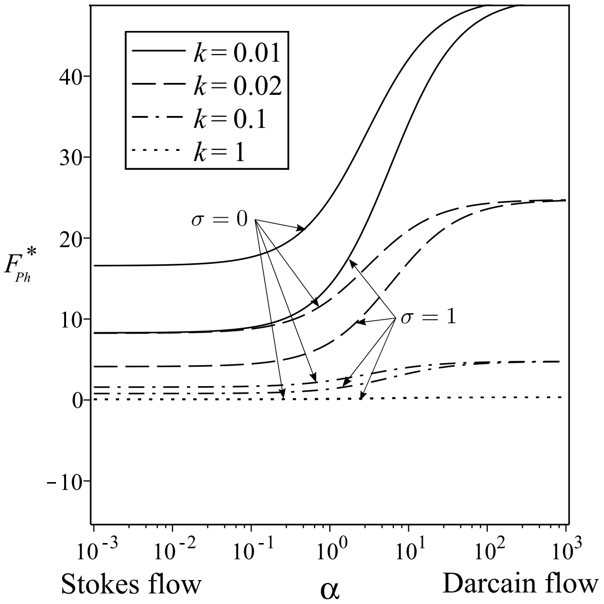

Figure 15: Normalized photocapillary force $F^*_{Ph}$ versus thermal conductivity ratio $k$ for different values of permeability parameter $\alpha$ at specific values of viscosity ratio $\sigma$ at ($\sigma = 0$ , $\sigma = 1$).

The non-dimensional photocapillary force, $F^*_{Ph}$, is examined in Figures 15 and 16 as a function of $\alpha$ for different $\sigma$ and $k$ values, respectively. For ($\alpha < 1$), $F^*_{Ph}$ shows no significant variation. As $\alpha$ increases into the range ($1 < \alpha < 100$), $F^*_{Ph}$ increases. For ($\alpha > 100$) (Darcian regime), $F^*_{Ph}$ tends towards a constant value. This saturation suggests that the drag exerted by the dense porous medium reaches a limit determined by the photocapillary driving mechanism. Figures 15 and 16 also indicate that for a given $\alpha$, $F^*_{Ph}$ increases as $\sigma$ or $k$ decreases.

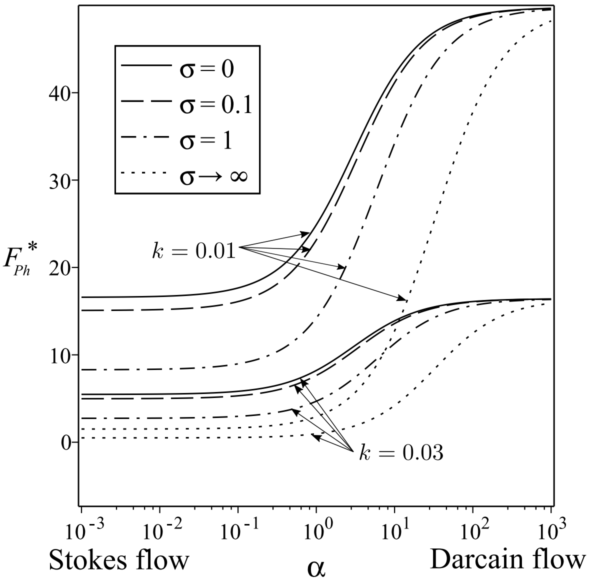

Figure 16: Normalized photocapillary force $F^*_{Ph}$ versus permeability parameter $\alpha$ for different values of viscosity ratio $\sigma$ at specific values thermal conductivity ratio ($k = 0.01$ , $k = 0.03$).

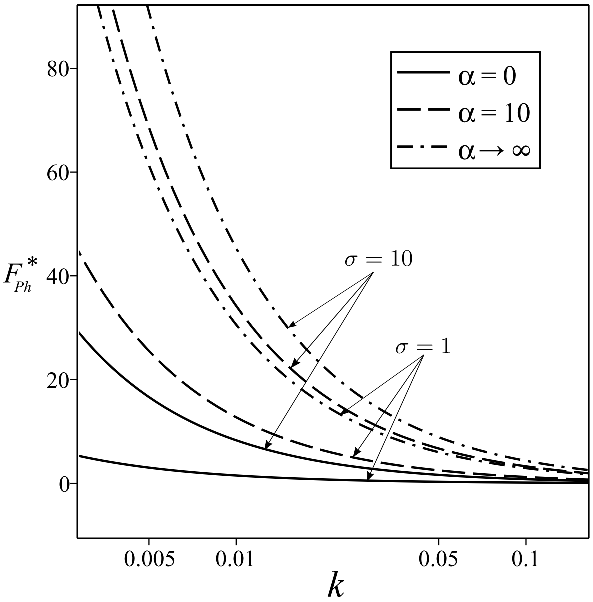

Figure 17: Normalized photocapillary force $F^*_{Ph}$ versus thermal conductivity ratio $k$ for different values of permeability parameter $\alpha$ at specific values of viscosity ratio $\sigma$ at ($\sigma = 1$ , $\sigma = 10$).

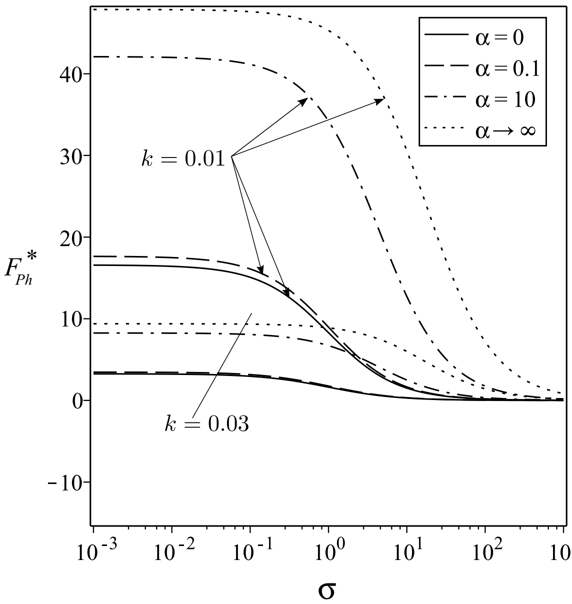

Figure 18: Normalized photocapillary force $F^*_{Ph}$ versus viscosity ratio $\sigma$ for different values of permeability parameter $\alpha$ at specific values of thermal conductivity ratio $k$ at ($k = 0.01$ , $k = 0.05$).

Fig. 17 illustrates the dependence of the normalized photocapillary force $F^*_{Ph}$ on the thermal conductivity ratio $k$, for various combinations of viscosity ratio $\sigma$ and permeability parameter $\alpha$. A particularly striking finding highlighted by this figure is the rapid decrease of $F^*_{Ph}$ towards zero within a very narrow range where ($k << 1$). This suggests that with the droplet being a considerably less efficient thermal conductor relative to the surrounding medium ($k << 1$), the development and sustenance of strong interfacial temperature gradients, essential for the Marangoni effect, are substantially diminished.

Fig. 18 provides a focused examination of the normalized photocapillary force $F^*_{Ph}$ as it varies with the viscosity ratio $\sigma$, specifically under conditions where the thermal conductivity ratio ($k << 1$). This condition ($k << 1$) signifies that the droplet is substantially less thermally conductive than the surrounding medium. The figure reveals a critical trend: $F^*_{Ph}$ tends towards zero as the viscosity ratio $\sigma$ becomes large (i.e., for highly viscous droplets), and this behavior holds true across the entire investigated range of the permeability parameter $\alpha$. The physical basis for this is quite direct: a droplet with high internal viscosity offers significant resistance to the internal fluid circulation that is essential for the Marangoni effect. These surface-tension-gradient-driven internal flows are strongly damped by high viscosity, consequently suppressing the propulsive Marangoni stress and, therefore, diminishing any resultant photocapillary force.

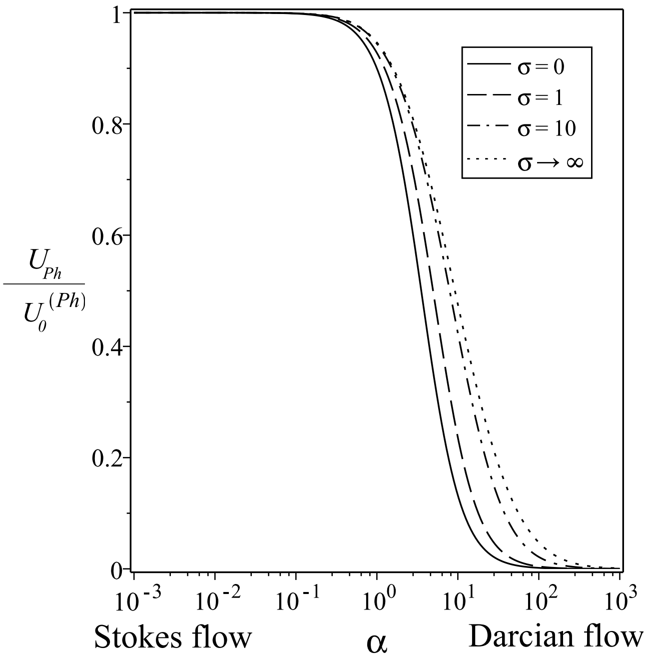

Figure 19: $U^*_{Ph}/U^{(0)}_{Ph}$ versus permeability parameter $\alpha$ for different values of viscosity ratio $\sigma$.

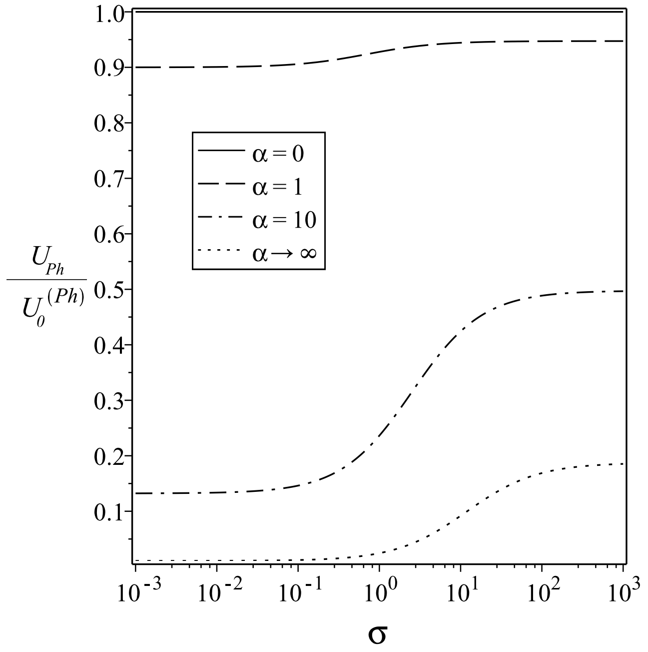

Figure 20: $U^*_{Ph}/U^{(0)}_{Ph}$ versus viscosity ratio $\sigma$ for different values of permeability parameter $\alpha$.

The normalized photocapillary velocity, $U_{Ph}/U_0^{(Ph)}$, where $U_0^{(Ph)}$ is the thermocapillary velocity in a clear viscous fluid (i.e., $\alpha = 0$), provides further insight. Fig. 19 plots $U_{Ph}/U_0^{(Ph)}$ against the permeability parameter $\alpha$ for various viscosity ratios $\sigma$. As expected, in the limit $\alpha \to 0$, the ratio $U_{Ph}/U_0^{(Ph)}$ approaches 1, recovering the clear fluid behavior. For ($\alpha < 1$), $U_{Ph}/U_0^{(Ph)}$ remains approximately 1 across the entire range of $\sigma$, confirming the negligible impact of the porous medium in this regime. This finding aligns with studies showing that for very high permeabilities, the Brinkman correction to Darcy's law, which accounts for viscous shear, becomes dominant and approaches Stokes flow behavior [28]. Consistent with the trend of$U^*_{Ph}$, Fig. 19 shows a sharp decrease in $U_{Ph}/U_0^{(Ph)}$ for ($1 < \alpha < 100$), eventually tending to zero for ($\alpha > 100$), highlighting the progressive attenuation of motion by the porous matrix. For a fixed $\alpha$ within this transitional range ($1 < \alpha < 100$), $U_{Ph}/U_0^{(Ph)}$ increases as $\sigma$ decreases. This implies that droplets with lower internal viscosity (relative to the external fluid) are more efficient at converting Marangoni stresses into motion, even when normalized against their clear fluid velocity.

Fig. 20 plots $U_{Ph}/U_0^{(Ph)}$ against the viscosity ratio $\sigma$ for various $\alpha$, corroborates these findings, illustrating a similar behavioral pattern to Fig. 19: increasing $\sigma$ (more viscous droplet) generally increases the normalized velocity, and for a fixed $\sigma$, the normalized velocity reduces as this reduction is more pronounced at higher $\alpha$ values where the porous medium's influence is stronger.

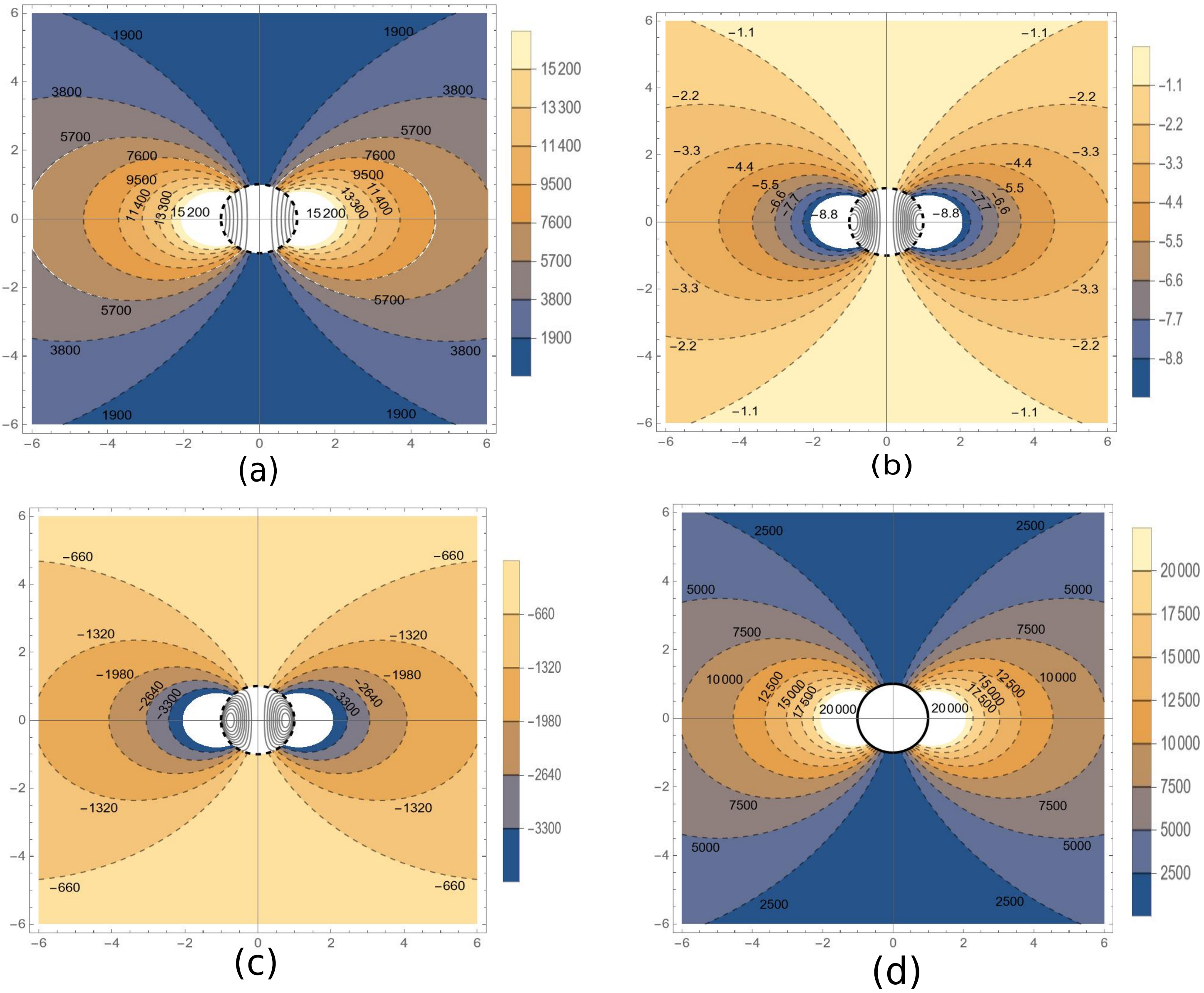

Figure 21: The streamline function is scaled with respect to $Ua^2$ for translational motion: $\tilde{\psi}^{(i)}/Ua^2 = C_2,\ i = d, p$, where $C_2$ is a constant. Each contour is found by assigning a specific value to the constant $C_2$, with (a) $\alpha \to 0,\ \sigma = 0.5,\ k = 1$, (b) $\alpha = 5,\ \sigma = 1,\ k = 0.155$, (c) $\alpha \to \infty,\ \sigma = 0.5,\ k = 0.01$, (d) $\alpha \to 0,\ \sigma \to \infty,\ k = 2$ (Solid Particle).

Fig. 21 similar to Fig. 12 shows the streamlines within the two regions $(r > a)$ and $(r < a)$. Again, the (a), (b) and (c) figures show the effects of the porosity parameter $\alpha$, the viscosity ratio $\sigma$ and the conductivity ratio $k$, and the solid particle case is shown in figure (d).

Table 1: Comparison between normalized thermocapillary velocity $U_T^*$ and normalized photocapillary velocity $U_{Ph}^*$ versus thermal conductivity ratio $k$, for different values of permeability parameter $\alpha$, at $\sigma = 1$.

| $\alpha$ | $k$ | $U_T^*$ | $U_{Ph}^*$ |
|---|---|---|---|
| $\alpha = 2$ | | | |
| | 0.5 | 0.129341317 | 0.086227545 |
| | 1 | 0.107784431 | 0.035928144 |
| | 1.5 | 0.092386655 | 0.020530368 |
| | 2 | 0.080838323 | 0.013473054 |
| | 2.5 | 0.071856287 | 0.009580838 |
| | 3 | 0.064670659 | 0.007185629 |
| | 3.5 | 0.058791508 | 0.005599191 |
| | 4 | 0.053892216 | 0.004491018 |
| | 4.5 | 0.049746661 | 0.003684938 |
| | 5 | 0.046193328 | 0.003079555 |
| $\alpha = 10$ | | | |
| | 0.5 | 0.037804296 | 0.025202864 |
| | 1 | 0.03150358 | 0.010501193 |
| | 1.5 | 0.027003069 | 0.006000682 |
| | 2 | 0.023627685 | 0.003937947 |
| | 2.5 | 0.021002387 | 0.002800318 |
| | 3 | 0.018902148 | 0.002100239 |
| | 3.5 | 0.017183771 | 0.00163655 |
| | 4 | 0.01575179 | 0.001312649 |
| | 4.5 | 0.014540114 | 0.001077045 |
| | 5 | 0.013501534 | 0.000900102 |
| $\alpha \to \infty$ | | | |
| | 0.5 | 0.000683109 | 0.000455406 |
| | 1 | 0.000569257 | 0.000189752 |
| | 1.5 | 0.000487935 | 0.00010843 |
| | 2 | 0.000426943 | 7.11572E-05 |
| | 2.5 | 0.000379505 | 5.06006E-05 |
| | 3 | 0.000341554 | 3.79505E-05 |
| | 3.5 | 0.000310504 | 2.95718E-05 |
| | 4 | 0.000284629 | 2.37191E-05 |
| | 4.5 | 0.000262734 | 1.94618E-05 |
| | 5 | 0.000243967 | 1.62645E-05 |

Table 2: Comparison between normalized thermocapillary force $F_T^*$ and normalized photocapillary force $F_{Ph}^*$ versus thermal conductivity ratio $k$, for different values of permeability parameter $\alpha$, at $\sigma = 1$.

| $\alpha$ | $k$ | $F_T^*$ | $F_{Ph}^*$ |
|---|---|---|---|
| $\alpha = 2$ | | | |
| | 0.05 | 0.182926829 | 3.658536585 |
| | 0.25 | 0.166666667 | 0.666666667 |
| | 0.45 | 0.153061224 | 0.340136054 |
| | 0.65 | 0.141509434 | 0.217706821 |
| | 0.85 | 0.131578947 | 0.154798762 |
| | 1.05 | 0.12295082 | 0.117096019 |
| | 1.25 | 0.115384615 | 0.092307692 |
| | 1.45 | 0.108695652 | 0.074962519 |
| | 1.65 | 0.102739726 | 0.062266501 |
| | 1.85 | 0.097402597 | 0.052650053 |
| | 2.05 | 0.092592593 | 0.045167118 |
| $\alpha = 10$ | | | |
| | 0.05 | 0.335365854 | 6.707317073 |
| | 0.25 | 0.305555556 | 1.222222222 |
| | 0.45 | 0.280612245 | 0.623582766 |
| | 0.65 | 0.259433962 | 0.399129173 |
| | 0.85 | 0.24122807 | 0.28379773 |
| | 1.05 | 0.225409836 | 0.214676034 |
| | 1.25 | 0.211538462 | 0.169230769 |
| | 1.45 | 0.199275362 | 0.137431284 |
| | 1.65 | 0.188356164 | 0.114155251 |
| | 1.85 | 0.178571429 | 0.096525097 |
| | 2.05 | 0.169753086 | 0.082806384 |
| $\alpha \to \infty$ | | | |
| | 0.05 | 0.464795214 | 9.29590428 |
| | 0.25 | 0.423480084 | 1.693920335 |
| | 0.45 | 0.388910281 | 0.864245069 |
| | 0.65 | 0.359558562 | 0.553167018 |
| | 0.85 | 0.334326382 | 0.393325155 |
| | 1.05 | 0.312403341 | 0.297526991 |
| | 1.25 | 0.29317852 | 0.234542816 |
| | 1.45 | 0.276182663 | 0.190470802 |
| | 1.65 | 0.261049367 | 0.158211737 |
| | 1.85 | 0.247488361 | 0.133777492 |
| | 2.05 | 0.235266713 | 0.11476425 |

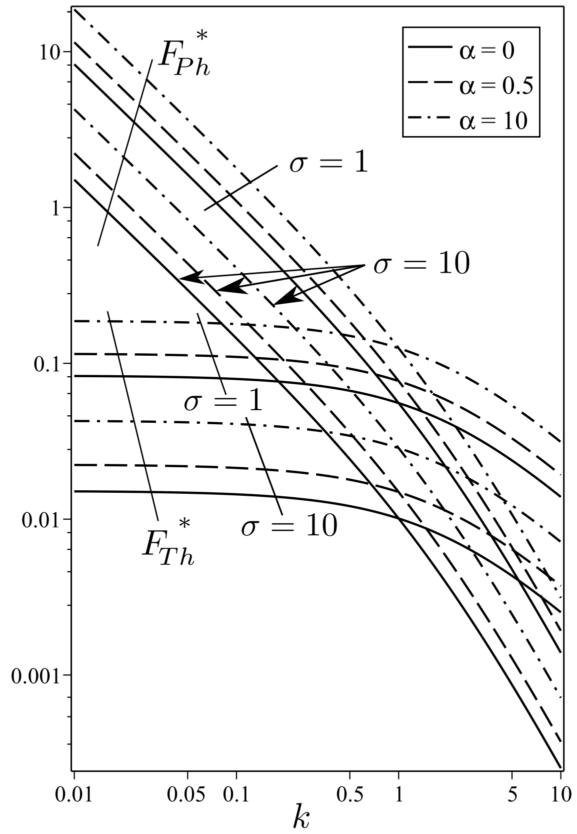

Figure 22: Comparison between normalized thermocapillary force $F_T^*$ and normalized photocapillary force $F_{Ph}^*$ versus thermal conductivity ratio $k$, for different values of permeability parameter $\alpha$, at specific values of viscosity ratio $\sigma = 1$ , $\sigma = 10$.

Table 1 displays the numeric comparison between the two normalized velocities due to the effects of thermocapillary $U_T^*$ and the photocapillary $U_{Ph}^*$. The two velocities are found for different values of the thermal conductivity ratio $k$ and the permeability parameter $\alpha$, at the viscosity ratio ($\sigma = 1$). It is observed that for fixed $\alpha$, both $U_T^*$ and $U_{Ph}^*$ decrease as $k$ increases, that is, a more thermally conductive droplet leads to lower interfacial temperature gradients, which in turn reduces Marangoni-driven motion, also, the photocapillary velocity drops more sharply than the thermocapillary velocity with increasing $k$, especially at low $\alpha$. For increasing $\alpha$, both $U_T^*$ and $U_{Ph}^*$ decline, approaching zero in the Darcian limit ($\alpha \to \infty$), and for any fixed $k$, it is obvious that the values of both velocities drop by more than two orders of magnitude as $\alpha$ increases from 2 to $\infty$, confirming the dominant drag of the porous structure. Table 2 shows the comparison between the normalized thermocapillary force $F_T^*$ and the normalized photocapillary force $F_{Ph}^*$, the same parametric attributes as Table 1 are present. The observable is that both forces decrease significantly with increasing $k$. For instance, at ($\alpha = 2$), $F_T^*$ drops by half, on the other hand, $F_{Ph}^*$ drops by a much larger magnitude. This again confirms that the low thermal conductivity of the droplet enhances temperature gradients, that is, stronger Marangoni stresses, that is, larger forces. At a fixed $k$, both forces increase with $\alpha$ (contrary to the velocities $U_T^*$, $U_{Ph}^*$). Larger $\alpha$ reflects to more hydrodynamic drag, so a greater driving force is required to maintain motion. Notably, despite the lower velocity, the force needed to move the droplet under photocapillary effect can be larger due to concentrated internal heating leading to stronger local stresses, but not necessarily higher net motion due to dissipation. A comparative analysis of the normalized thermocapillary force $F_T^*$ and photocapillary force $F_{Ph}^*$ versus the thermal conductivity ratio $k$, as depicted in Fig. 22, reveals distinct behaviors rooted in their mechanisms of interfacial temperature gradient generation. $F_T^*$, arising from an externally imposed thermal field, exhibits a monotonic decrease with an increasing $k$; a higher $k$ signifies a more thermally conductive droplet relative to its surroundings, leading to enhanced heat diffusion through the droplet bulk, which homogenizes the droplet's internal temperature and thereby diminishes the magnitude of the temperature gradient sustained along its interface by the external field, consequently weakening Marangoni stresses and reducing the propulsive force. Conversely, $F_{Ph}^*$, generated by internal heat absorption from light, displays a particularly striking rapid decrease towards zero within a very narrow range where ($k << 1$). This occurs because when the droplet is a considerably less efficient thermal conductor (both internally and relative to the surrounding medium), the heat generated within it cannot effectively establish and sustain strong interfacial temperature gradients necessary for a significant Marangoni effect; the poor internal thermal transport delays the development of a non-uniform surface temperature profile. Thus, at ($k << 1$), $F_T^*$ tends to be relatively high as the droplet's poor conductivity helps maintain the externally imposed gradient across its interface, while $F_{Ph}^*$ drops because the same poor conductivity prevents internally generated heat from creating an effective interfacial gradient. The permeability parameter $\alpha$ primarily impacts $F_{Ph}^*$, where increasing $\alpha$ (from 0 to 10) significantly enhances $F_{Ph}^*$, likely due to improved internal convective heat transfer which aids in establishing stronger interfacial temperature gradients from the absorbed light; while its impact on $F_T^*$ is less direct unless it significantly alters the bulk effective thermal conductivity. Notably, $F_{Ph}^*$ generally achieves considerably larger magnitudes than $F_T^*$, particularly at lower $\sigma$ and higher $\alpha$, highlighting the potential for internal light absorption, aided by permeability, to generate more potent Marangoni propulsion than external thermal fields, though this advantage diminishes significantly when the droplet's thermal conductivity $k$ is extremely low.

## 6. Conclusion

In conclusion, this investigation delineates the fundamentally divergent behaviors of thermocapillary and photocapillary droplet migration within a saturated porous matrix, establishing a predictive analytical framework based on the Brinkman equation. Our analysis rigorously demonstrates that the externally-driven thermocapillary velocity $U_T^*$ is invariably attenuated by increasing matrix resistance (permeability parameter $\alpha$), droplet-to-medium thermal conductivity ratio $k$, and viscosity ratio $\sigma$ attributable respectively to intensified Darcy drag, interfacial thermal homogenization that erodes the driving gradient, and heightened internal viscous dissipation. Significantly, we reveal that high matrix resistance not only severely suppresses $U_T^*$ but also diminishes its sensitivity to viscosity by effectively immobilizing the interface and promoting internal thermal equilibration. In stark contrast, while the internally-driven photocapillary velocity $U_{Ph}^*$ is similarly retarded by matrix resistance and high internal viscosity, its propulsive mechanism is critically predicated on the droplet's ability to establish its own interfacial thermal gradient. Consequently, the associated photocapillary force $F_{Ph}^*$ is extinguished at low thermal conductivity ratios $k << 1$ where internal heat distribution is ineffectual. This establishes a key mechanistic dichotomy: whereas the thermocapillary force $F_T^*$ monotonically weakens with increasing $k$, the photocapillary force $F_{Ph}^*$ exhibits a greater sensitivity to matrix permeability, which modulates the internal convection essential for distributing absorbed energy, and can achieve superior magnitudes. However, this potential advantage is strictly contingent upon sufficient droplet thermal conductivity for the efficient conversion of absorbed volumetric energy into a potent surface tension gradient. Ultimately, this research provides a comprehensive framework detailing the intricate interplay between porous confinement, thermophysical properties, and the locus of the thermal stimulus, offering foundational principles for the design and control of Marangoni-actuated transport in complex multiphase systems.

## 7. Conflict of interest

We have no conflict of interest to declare.

## References

[1] L. Zhang, R.S. Subramanian, and R. Balasubramaniam. Motion of a drop in a vertical temperature gradient at small marangoni number–the critical role of inertia. *Journal of Fluid Mechanics*, 448:197–211, 2001.

[2] P.-G. De Gennes, F. Brochard-Wyart, and D. Quéré. Capillarity and wetting phenomena: drops, bubbles, pearls, waves. 2003.

[3] A. Ebrahimi, Y. Kazemzadeh, and A. Akbari. Impact of the marangoni phenomenon on the different enhanced oil recovery methods. *Heliyon*, 10(21):e39919, 2024.

[4] R.S. Subramanian, R. Balasubramaniam, and N. Clark. Motion of bubbles and drops in reduced gravity. *Appl. Mech. Rev.*, 55(3):B56–B57, 2002.

[5] B. Selva, I. Cantat, and M.-C. Jullien. Temperature-induced migration of a bubble in a soft microcavity. *Physics of fluids*, 23(5), 2011.

[6] N. Young, J.S. Goldstein, and M. Block. The motion of bubbles in a vertical temperature gradient. *Journal of Fluid Mechanics*, 6(3):350–356, 1959.

[7] M. Meyyappan, W.R. Wilcox, and R.S. Subramanian. Thermocapillary migration of a bubble normal to a plane surface. *Journal of Colloid and Interface Science*, 83(1):199–208, 1981.

[8] M. Meyyappan, W.R. Wilcox, and R.S. Subramanian. The slow axisymmetric motion of two bubbles in a thermal gradient. *Journal of Colloid and Interface Science*, 94(1):243–257, 1983.

[9] J.L. Anderson. Droplet interactions in thermocapillary motion. *International journal of multiphase flow*, 11(6):813–824, 1985.

[10] A. Acrivos, D. Jeffrey, and D. Saville. Particle migration in suspensions by thermocapillary or electrophoretic motion. *Journal of Fluid Mechanics*, 212:95–110, 1990.

[11] D.S. Morton, R.S. Subramanian, and R. Balasubramaniam. The migration of a compound drop due to thermocapillarity. *Physics of Fluids A: Fluid Dynamics*, 2(12):2119–2133, 1990.

[12] S.S. Sadhal. A note on the thermocapillary migration of a bubble normal to a plane surface. *Journal of colloid and interface science*, 95(1):283–285, 1983.

[13] M. Meyyappan and R.S. Subramanian. Thermocapillary migration of a gas bubble in an arbitrary direction with respect to a plane surface. *Journal of colloid and interface science*, 115(1):206–219, 1987.

[14] MS Faltas, HH Sherief, Allam A Allam, MG Nashwan, and M El-Sayed. Thermophoresis of a spherical particle in a permeable microchannel with thermal stress slip. *Physical Review Fluids*, 8(5):054102, 2023.

[15] MS Faltas, HH Sherief, EI Saad, and AS Aamer. Migration of a porous spherical particle in the presence of a non-deformable interface. *European Journal of Mechanics-B/Fluids*, page 204277, 2025.

[16] K.D. Barton and R.S. Subramanian. Thermocapillary migration of a liquid drop normal to a plane surface. *Journal of colloid and interface science*, 137(1):170–182, 1990.

[17] S.H. Chen and H.J. Keh. Thermocapillary motion of a fluid droplet normal to a plane surface. *Journal of colloid and interface science*, 137(2):550–562, 1990.

[18] K.D. Barton and R.S. Subramanian. Migration of liquid drops in a vertical temperature gradient—interaction effects near a horizontal surface. *Journal of colloid and interface science*, 141(1):146–156, 1991.

[19] Y.C. Chang and H.J. Keh. Thermocapillary motion of a fluid droplet perpendicular to two plane walls. *Chemical engineering science*, 61(16):5221–5235, 2006.

[20] T.C. Lee and H.J. Keh. Axisymmetric thermocapillary migration of a fluid sphere in a spherical cavity. *International Journal of Heat and Mass Transfer*, 62:772–781, 2013.

[21] T.C. Lee and H.J. Keh. Thermocapillary motion of a spherical drop in a spherical cavity. *CMES*, 93:317–333, 2013.

[22] M. Loewenberg and R.H. Davis. Near-contact, thermocapillary migration of a nonconducting, viscous drop normal to a planar interface. *Journal of colloid and interface science*, 160(2):265–274, 1993.

[23] S.H. Chen. Thermocapillary deposition of a fluid droplet normal to a planar surface. *Langmuir*, 15(8):2674–2683, 1999.

[24] H.J. Keh, P.Y. Chen, and L.S. Chen. Thermocapillary motion of a fluid droplet parallel to two plane walls. *International journal of multiphase flow*, 28(7):1149–

1175, 2002.

[25] D. Choudhuri and G.P. Raja Sekhar. Thermocapillary drift on a spherical drop in a viscous fluid. *Physics of Fluids*, 25(4), 2013.

[26] H.C. Chiu and H.J. Keh. Thermocapillary migration of a fluid sphere in a circular tube. *American Journal of Heat and Mass Transfer*, 3(1):15–36, 2016.

[27] D. Chennuri and J. Prakash. Thermocapillary migration of a compound drop in an arbitrary viscous flow. *European Journal of Mechanics - B/Fluids*, 106:280–289, 2024.

[28] H.C. Brinkman. A calculation of the viscous force exerted by a flowing fluid on a dense swarm of particles. *Flow, Turbulence and Combustion*, 1(1):27–34, 1949.

[29] Larry D. Reed. Low knudsen number photophoresis. *Journal of Aerosol Science*, 8(2):123–131, 1977.

[30] Yu Chen Chang and Huan J. Keh. Thermophoresis at small but finite péclet numbers. *Aerosol Science and Technology*, 52(9):1028–1036, 2018.

[31] Christopher J. Lawrence and Sheldon Weinbaum. The unsteady force on a body at low reynolds number; the axisymmetric motion of a spheroid. *Journal of Fluid Mechanics*, 189:463–489, 1988.

[32] DW Mackowski. Photophoresis of aerosol particles in the free molecular and slip-flow regimes. *International Journal of Heat and Mass Transfer*, 32(5):843–854, 1989.

[33] MS Faltas and Kareem E Ragab. Thermophoretic and photophoretic velocities and forces of a spherical particle embedded in brinkman medium. *The European Physical Journal Plus*, 134(9):475, 2019.

[34] Peter W Dusel, Milton Kerker, and Derry D Cooke. Distribution of absorption centers within irradiated spheres. *Journal of the Optical Society of America*, 69(1):55–59, 1979.

[35] H. Haj-Hariri, A. Nadim, and A. Borhan. Effect of inertia on the thermocapillary velocity of a drop. *Journal of Colloid and Interface Science*, 140(1):277–286, 1990.

[36] Donald A. Nield and Adrian Bejan. *Convection in Porous Media.* Springer, 5th edition, 2017.

[37] E.S. Nasibullaeva and S. Urmancheev. Thermocapillary migration of droplets and bubbles in a viscous liquid (review). *Multiphase Systems*, 15:144–158, 2020.